POLITECNICO DI MILANO
DEPARTMENT OF PHYSICS
DOCTORAL PROGRAMME IN PHYSICS

Anion intercalation in graphite:

a combined Electrochemical Atomic Force and Scanning Tunneling Microscopy investigation

Doctoral Dissertation of:
Rossella Yivlialin

Supervisor:
Dr. Gianlorenzo Bussetti

Tutor:
Prof. Franco Ciccacci

The Chair of the Doctoral Program:
Prof. Paola Taroni

24th February 2017 – XXIX cycle

To my parents

ABSTRACT

Graphite electrodes have been, and continue to be, used largely in electrochemistry for a wide range of applications from energy conversion or storage (e.g. lithium-ion batteries and fuel cells) to electronic analysis (e.g. DNA analysis by carbon electronic chips) and in a wide range of sizes, from micron or submicron to electrodes with extension of square meters.

Electrochemistry has been connected to graphite since the early days of its research activity because of its good electrical and thermal conductivity, corrosion resistance, low thermal expansion, low elasticity and high purity. The more traditional form of graphite implemented as electrode is the Highly Oriented Pyrolytic Graphite (HOPG) crystal. Nowadays, HOPG has also focused an additional increasing interest due to its layered structure, which can be thought in terms of a graphene sheet pile. In view of industrial implementation, we are obliged to combine a quantity and quality enhancement of graphene together with a reduction of the cost production. In these perspectives, electrochemical strategies are successful. Graphite is delaminated by anion intercalation inside the crystal at specific electrochemical potentials. Anions are placed in the inter-layer region and they expand the graphite structure of about a factor of 3. Consequently, the layer-layer interaction is reduced and a gentle sonication dissolves part of the original HOPG crystal inside a suspension of graphene sheets. Despite good results are reported and discussed in the literature, the graphene sheet sizes are wide dispersed over a range of 2 order of magnitudes (radii from tens of nanometers up to 1 micrometer are observed). In addition, structural damages, defects, water and electrolyte contaminations are frequently reported. Most of the works follow a trial-and-error method but it has been recently noted that there is an unjustified lack of knowledges, regarding the molecular mechanisms involved during anion intercalation in graphite. An explanation of the HOPG delamination steps can help in a further optimization of the production protocol.

This PhD thesis exploits an electrochemical scanning probe microscopy (EC-SPM) to disclose the first stages of sulfuric and perchloric intercalation in graphite. The EC-SPM combines a traditional three-electrode cell with both an atomic force and scanning tunneling microscopy (AFM and STM, respectively) and is able to characterize the morphology and local structure of the electrode surface as a function of the EC potential, *in-situ* and in real time (during the EC potential changes). A traditional cyclic-voltammetry (CV), where the sample EC potential is ramped linearly versus time and the flowing current accordingly measured, allows a characterization of the electrolytes and ensures that EC processes occur at the graphite electrode surface.

In this research, I proved that the graphite basal plane is damaged when high anodic potentials are selected for the sample electrode. A carbon dissolution erodes graphite step edges or produces deep holes on surfaces. These processes are a clear detriment in view of graphene production, because the sheets show defects even before the graphite delamination. In addition, the HOPG electrode is affected by blisters, as soon as the oxygen overpotential is reached during the CV in both H_2SO_4 and $HClO_4$. Blisters swell the graphite surface and stretches the C-C bonds of few percent, promoting other structural lacerations.

Blister evolution seems to be related to the oxidation of solvated anions and to a subsequent evolution of gases (namely CO, CO_2 and O_2). A compared analysis, driven at different EC potential, allows the definition of a new intercalation model, proposed in this thesis. When the oxygen overpotential is reached during the CV, OH^- anions penetrate inside HOPG and exchange an electron charge at the electrode-electrolyte interface. Oxygen is produced and the graphite surface partially swells. A further increase in the EC potential favors the sulfuric and perchlorate anion intercalation and a concomitant dissolution of carbon. CO and CO_2 are produced and wide areas of HOPG are affected by blisters.

I believe that these findings shine a first light on the molecular mechanism involved during anion intercalation, helping technology to optimize the graphene production protocols. In particular, intercalation must be obtained with concentrated acids to avoid a

percolation of solvated anions that favor the blister evolution. On the other hand, hydroxyl group intercalation is still enough to swell graphite and helping the graphite delamination. Interestingly, I observe that this process occurs before the anion intercalation, limiting the crystal detriment due to graphite dissolution.

CONTENTS

LIST OF FIGURES

1 INTRODUCTION

Electrode reactions are heterogeneous and take place at the interface between electrode and solution. Among different electrodes, carbon-based electrodes have been, and continue to be, used largely in electrochemistry, for a wide range of applications: from energy conversion or storage (e.g. lithium-ion batteries and fuel cells [1]), to electronic analysis (e.g. DNA analysis by carbon electronic chips [2]) and in a wide range of sizes, from micron or submicron to extension of square meters.

Electrochemistry has been connected to carbon materials since the early days of its research activity [3] because of its good electrical and thermal conductivity, corrosion resistance, low thermal expansion, low elasticity and high purity. Furthermore, carbon can be produced in different forms (e.g. graphite, diamond, graphene, carbon nanotube and graphene nanoribbon), whose electronic and functionalization properties have been largely investigated [4,5].

The more diffused form of carbon is graphite, which has been used as an active electrode in many studies, such as the creation of nanoscale interfaces for sensing and biological applications [6] or as model system for heterogeneous metal deposition and nucleation growth [7].

Since the Nobel Prize in physics to A. Gejm and K. Novoselov (2010), we can re-interpret graphite as the nature's way to build up stacks of graphene (single monoatomic graphite layers) into a bulk crystal. In graphene, carbon atoms form regular sheets of linked hexagon, which are displaced one to another relatively. These sheets can adopt two possible arrangements or stacking order in graphite: hexagonal (the more diffuse in nature) and rhombohedral, which is unstable and, consequently, less common in nature. The type of stacking has important implications for the graphite electronic properties [8], even though the stacking distance between two consecutive layers is 0.35 nm [9], in both arrangements.

The crystal structures are displayed in **Figure 1** and consists of carbon honeycomb planes stacked along the *c*-axis in an ABA or ABC configuration. The lateral shift of layer B from layer A is 0.25 nm [9].

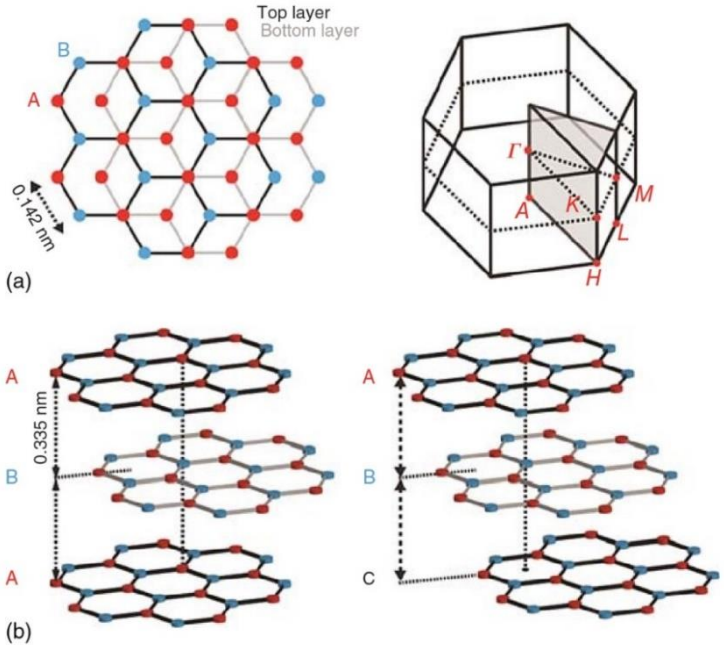

***Figure 1**. a) Top view and unit cell in the reciprocal space of the hexagonal graphite crystal structure: A and B are in plane carbon atoms. b) Lateral view of hexagonal and rhombohedral graphite. A, B and C are honeycomb single planes. The ABA and ABC stacking are displayed.*

Within the layers, each carbon atom –hybridized sp^2- is linked by a strong covalent σ-bond with three neighbors, placed at a distance of 0.14 nm [10]. These bonds are responsible for the planar structure of graphene and for the noticeable mechanical and thermal properties.

The carbon valence electrons half-fill the $2p_z$ orbital, which is orthogonal to the graphene plane and forms a weak (van der Waals) π-bond along the z-direction, by overlapping with other $2p_z$ orbitals that belong to a neighbor graphene layer.

To take full advantage from the properties of the hexagonal structure, a very common form of artificial graphite crystal, i.e. the Highly Oriented Pyrolytic Graphite (HOPG), is exploited for scientific and industrial purposes. It origins from pyrolytic graphite that is produced by the thermal decomposition of carbonaceous gases in petroleum coke, usually methane, at temperatures above 1200°C. When the pyrolytic carbon is heated again at high temperatures but under high pressure, the HOPG is produced [11]. HOPG is a polycrystalline material formed by many graphite monocrystals, each of them composed by graphite flakes (or grains) of different sizes [12]. The crystallographic orientation of the *c*-axes changes from a mono-crystal to another one and the *mosaic spread* parameter (i.e. the angular parameter) quantifies the degree of reciprocal misorientation of graphene layers: the lower the mosaic spread, the higher the quality of HOPG. In this respect, HOPG quality is categorized with a grade terminology that depends on the supplier: the highest quality is termed ZYA with mosaic spread of $0.4 \pm 0.1°$. HOPG grades of lower quality are ZYB (mosaic spread $0.8 \pm 0.2°$), ZYD ($1.2 \pm 0.2°$) and ZYH grades ($3.5 \pm 1.5°$) [13]. The layered structure of HOPG, regardless the crystal grade, shows a significant mechanical anisotropy, which results in an easy delamination along the z-axis [14,15]. As a consequence, HOPG is particularly suitable for providing wide areas of atomically flat surfaces by simple exfoliation. The use of adhesive tape to peel off the first crystal layers, obtaining a fresh and atomically flat surface, is the most common procedure [16], even though there are other mechanical cleavage techniques (e.g. by ultrasharp diamond wedges [17]). The out-of-plane π orbitals low interact with the environment, maintaining the graphite surface almost clean for several minutes. Due to these advantages, HOPG is suitable for atomic-resolution microscopies, such as Scanning Tunneling Microscopy [18] (STM) and Atomic Force Microscopy [19] (AFM).

The mechanical, thermal and chemical stability of graphite makes HOPG of great interest as electrode in traditional electrochemical cells [20]. For this reason, wide formative studies about the electrochemistry of HOPG were conducted in the past, in view of understanding the role of both the basal plane and the surface defects in reactions [20,21]. Differences between the allotropic forms of carbon materials (i.e. HOPG, nanotube, nanowires, graphene, etc.) are still under investigation [22-24].

The investigation of the basal plane and surface defect electroactivity is also crucial to evaluate the applicability of HOPG in commercial devices (e.g. ion transfer batteries). The redox processes[1] occurring on the HOPG-electrolyte interface have been followed by different techniques (potentiostatic, polarographic, diffractive, optical, etc.) and under different solutions. To improve its performances, HOPG is usually implemented as substrate in heterogeneous systems or combined with redox active molecules (e.g. $Fe(CN)^{-3/-4}$) [25].

Relevant characteristics of such kind of systems have been discovered by combining traditional STM and AFM techniques with other ones, more closely related to electrochemistry and, in particular, with the so-called cyclic-voltammetry (CV) [26].The latter is a particular potentiodynamic measurement, where the sample potential is linearly ramped versus time and the flowing current is plotted versus the applied voltage. This technical combination, exploited for the experimental investigations presented in this thesis, will be exposed in-depth in the following sections.

Despite the good stability of graphite as electrode, some electrolytes are able to intercalate inside the HOPG stratified structure, screening the layer-layer

[1] A reduction-oxidation (redox) process indicates a chemical reaction that involves electron exchange from a considered chemical specie (atom or molecule) to another one. Reduction and oxidation are two contemporaneous semi-reactions: the chemical specie giving electrons is oxidized, while the chemical specie accepting the electrons is reduced.

interaction and helping the crystal delamination in aqueous solutions [27]. This occurrence has been extensively exploited by the industrial field of flat flexible electronics, where graphene is largely used. The important results reported in the literature [28,29], encourage to extend electrochemical strategies to the wide class of layered crystals, such as MoS_2, MnO_2, etc. [30], even if just few results are already available on this topic, probably because it is difficult to find the proper electrolyte. In HOPG intercalation, by applying a suitable electrochemical (EC) potential to the graphite sample immersed in an aqueous acid solution, the ions are forced to intercalate within the graphite layers [31]. The main advantages of this method consist in the possibility of choosing the starting time and the kinetics of the process. Traditional electrolytes are sulfuric (H_2SO_4), perchloric ($HClO_4$) and nitric (HNO_3) acids. These solutions have strong oxidation effects, which could generate defects in exfoliated graphene sheets. To reduce this drawback, other electrolytes (sulfonate salts, alkaline solutions and phosphate buffer solution) are to date chosen as intercalating agents [29,31].

After intercalation, a gentle sonication helps the HOPG delamination and graphene sheets production. The latter are dispersed in a solution and sold for many purposes. Graphene is found oxidized (GO) and shows typical lateral dimensions of hundreds of nanometers, but a crucial point is the structural quality of the produced sheets for effective application in electronics. For this reason, many studies have been focused on the characterization of the produced graphene flakes [32].

Nonetheless, I believe that a concrete improvement of the electrochemical exfoliation strategy and, consequently, of the so produced graphene quality could result from understanding the molecular mechanism of ion intercalation in the graphite mother crystal, at the nano/micrometer scale. In fact, the same HOPG is used for several continued intercalation/exfoliation cycles, to obtain large amounts of graphene. The progressive detriment of the pristine crystal affects the

final graphene quality. A better knowledge of this process clearly helps the optimization of the HOPG delamination protocol.

The electrochemical principles of the acid intercalation process in graphite have been already studied in the past [3,33,34]. Acid ions penetrate at precise potentials into the gaps between the carbon layers and enlarge the interlayer graphite distance. Charges are accepted into the carbon host lattice, according to the equations 1.1 [3], which describe both a cathodic and an anodic process:

$$[C_x] + [M^+] + e^- = C_x^- + M^+$$

$$[C_x] + [A^-] = C_x^+ + A^- + e^- \qquad (1.1)$$

where M^+ is a cation and A^- an anion. C_x represents a stoichiometric amount of graphite carbon atoms involved in the charge-transfer with the electrolyte solution.

The product of the intercalation process is called Graphite Intercalation Compounds (GIC), which affects the uppermost layers of the graphite crystal. The GIC structure is tentatively described by a model that suggests the creation of a statistically regular array of occupied/unoccupied layers, also called stage formation [34-36]. In a GIC stage n, for example, inter-layers containing intercalated ions are separated by (n-1) uncontaminated inter-layers. The diagram in **Figure 2** shows 4 consecutive stages:

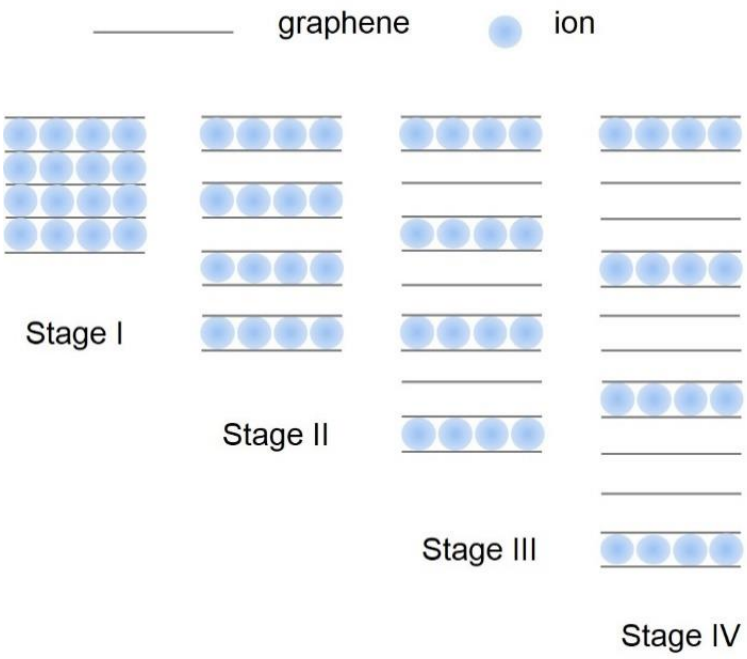

***Figure 2**. Schematic representation of the intercalation stage in four different GIC configurations. Grey line is the carbon layer and balls represent the intercalated ions.*

Because many electrolytes are water-based solutions and the solvent can intercalate into the graphite lattice, the GIC model foresees a refinement. Here, a ternary phase $[C_x^+A^-]y(solv.)$ is produced according to equation 1.2, where A^- is an anion (a similar equation describes solvated-cations intercalation).

$$[C_x] + [A^-] + y(solv.) = [C_x^+A^-]y(solv.) + e^- \quad (1.2)$$

Due to the degree of solvation (i.e. the ratio between acid ions and solvent molecules, expressed by y in eq. 1.2), different molecular configurations are possible. These are collected in two main groups: three-dimensional (3D) and two-dimensional (2D) solvated phase, as represented in **Figure 3** [36].

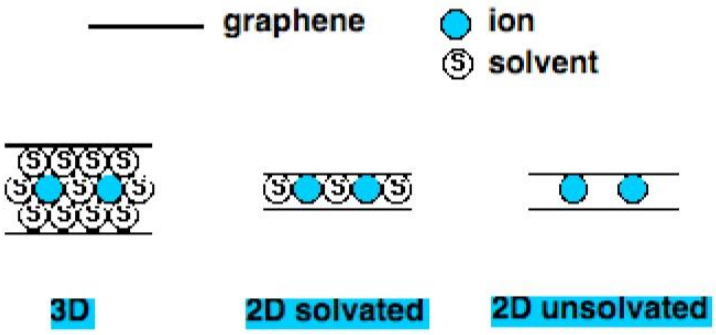

***Figure 3**. Schematic representation of 3D and 2D solvated intercalated ions in graphite. S is for solvent, solid balls are for ions, solid line is for carbon layer [36]. The basic 2D unsolvated model is reported for comparison.*

In the 2D solvated phase, the distance between the carbon layers is determined either by the size of the solvent molecule or by the size of the ion [37].

Low-index GIC stages are easily obtained during graphite oxidation. In this case, HOPG is positive biased, with respect to a standard hydrogen electrode (SHE), at quite high electrochemical (EC) potentials (order of volts), i.e. close to the oxygen evolution of the graphite electrode. The anodic behavior of HOPG varies with the specific used electrolytes. These are collected in two acid classes [33], whose name belongs from one of the elements of the ensemble: the phosphoric acid group (e.g. H_3PO_4, HCl, etc.) and the sulfuric acid group (i.e. H_2SO_4, $HClO_4$, etc.). When graphite is immersed in an electrolyte of the first group and a high EC potential is applied, the basal plane is attacked by the oxidation processes and carbon dissolution is probable. These phenomena are expected for electrolytes belong to the second class, too. In addition, H_2SO_4-group swells the HOPG surface and damages the internal graphite structure [38-40].

The crystal evolution is even more complicated when traditionally diluted acids (2 M or less) are used as electrolytes, as pointed out by Alsmeyer and McCreery

[41]. The authors investigated the relationship between intercalation processes and side reactions, such as oxidation, and proposed that graphite oxides (GO) follow the firstly GIC formation. On the other hand, surface bubbles (called blisters) evolve on the HOPG surface after anion intercalation as proved by AFM [31,36,39] and STM [42] investigations. While a carbon dissolution is foreseen in concentrated acids, in diluted electrolytes no damages of the graphite surface are reported at low (i.e. in the double-layer region[2]) electrode potentials [43,44], yet.

In this tangled context, Royce W. Murray and co. workers succeeded in summarizing the experimental results in an original interpretative model of intercalated HOPG in diluted electrolytic solutions [40]. **Figure 4** shows different steps of the HOPG anion intercalation according to the Murray's model: electrochemical GO (EGO) formation, GIC phase and blister evolution are clearly reported. Two basic ideas characterize the model: i) crystal defects (steps, grain borders, holes, kinks, adatoms, valleys) are a direct access to anions; ii) inter-layer spacing allows the intercalation of solvated anions. Under these hypotheses, solvated anions oxidize carbon, as soon as high EC potentials are applied to the graphite electrode. The HOPG oxidation produces specific gases (CO, CO_2, O_2) that start to swell the graphite surface, resulting in the blister formation (see panel C). The blister size is contained by the graphite layer (graphene) strain, which stabilizes the surface morphology, as reported in D.

[2] Electrochemical potential interval in which the electrode-solution interface is modelled as a capacitor system, called Helmotz double-layer.

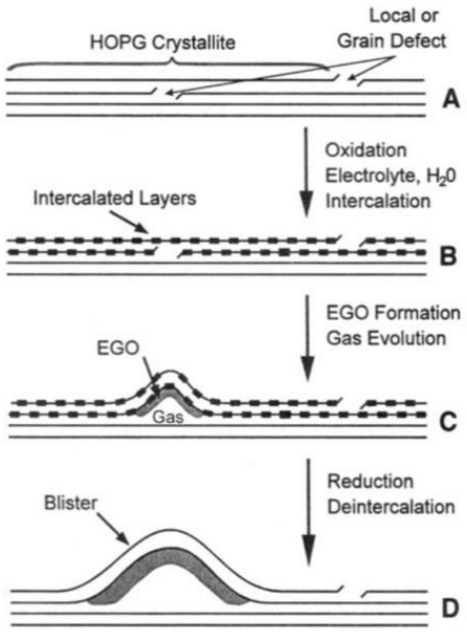

***Figure 4**. Model of blister formation and growth: A) cross section of the basal HOPG plane before the oxidation. Lines correspond to HOPG layers (graphene). Surface and bulk defect sites (e.g. crystalline grain boundaries, step edges, etc.) are also depicted. B) when HOPG is positively biased, carbon oxidation takes place. Dashed lines indicate areas where solvated anion intercalation occurred. C) initial blister growth. The shaded area represents graphite oxide. D) final and stable blister structure.*

Murray model becomes insufficient when mechanisms at the nano-scale are investigated, opening new intriguing questions. For example, are surface defects concrete accesses of solvated anions? At the EC potentials used for intercalation, is there a carbon dissolution that helps the formation of defects? Is the GIC structure different with respect to the pristine HOPG? Are CO, CO_2, O_2 produced together and at the same time? Are blister really stable or not? What is the timing (chemical kinetics) of anion intercalation and blister formation? These questions require urgent answers in view of stopping, or at least attenuating, graphite detriment in acid electrolyte, which significantly limits the quality of graphene flakes, produced by the EC strategy. To this goal, preliminary results were obtained *in-situ* (i.e. inside an EC cell) by using special AFM systems (known as EC-AFM). In particular, as reported in Ref. 44, an HOPG electrode

was efficiently intercalated, by using a traditional CV, and the *a posteriori* morphology of the graphite surface was observed by the EC-AFM at a defined EC potential and without removing the electrolyte solution. The authors succeeded in a GIC morphology characterization at the sub-micrometer scale, in agreement with the Murray model. Nonetheless, the experimental approach, the investigated EC potential range, the AFM lateral size resolution, the chosen electrolytes, etc. are insufficient to give a conclusive answer to the above reported questions. I believe that an improvement of our knowledge of the graphite intercalation process requires an *in-situ* atomic-resolution technique coupled with a different EC strategy, which should help in monitoring the process time-scale. In this way, we can trust to refine the Murray model for the interpretation of the local phenomena as a function of time.

In this thesis, HOPG is immersed in diluted electrolytes that belong to both the two acid classes, in view of a direct comparison between their intercalation effects. The traditional CV is sustained by normal pulse voltammetry (NPV), where the EC potential is rapidly changed from a starting value to the chosen potential for a well-defined time interval. Consequently, anion intercalation kinetics can be disclosed, for the first time, by the NPV. The latter, in fact, can monitor fast changes (tens of microseconds) in the measured faradic currents. Finally, the EC-AFM is sustained by EC-STM to succeed in the atomic-structure resolution of the GIC.

The experimental data show that concomitant processes affect the pristine HOPG surface, as soon as the faradaic current flows across the sample. These processes can be distinguished if the NPV is applied at different EC potentials. In particular, graphite blistering, observed with diluted electrolytes belonging to the sulfuric acid class, ramp down as a high EC potential is applied to the graphite electrode. Conversely, blister growth time can be minimized, if a proper EC

potential is set. In this case, I speculate that only O_2 gas is trapped below the HOPG surface, as discussed in this thesis.

These results help for a better comprehension of the molecular mechanisms, acting during anion intercalation, and allow a significant refinement of the Murray model for a better interpretation of experimental data at the nanometer scale. I believe that the findings presented and discussed in this thesis could be helpful in the HOPG delamination protocol optimization, in view of an important enhancement of the industrial and technological graphene production quality.

2 EXPERIMENTAL TECHNIQUES

2.1 *ELECTROCHEMISTRY*

2.1.1 GENERAL DETAILS

Electrochemical techniques are fundamental tools for oxidation[3] and reduction[4] process studies. They are commonly used to study kinetics and thermodynamics of electron and ion transfer processes [45]. Electrochemical techniques have been proven to be useful tools, even for the study of adsorption and crystallization phenomena at the electrode surfaces [46]. Their wide application is attributed to the relatively compact instrumentation available nowadays, the high sensitivity in wide concentration ranges, for both inorganic and organic compounds, and the fast analysis scans (in the order of milliseconds) [47].

Electrochemical techniques are divided into static (e.g. potentiometry) and dynamic, where EC potential or faradic current (coulometry) can be controlled [48]. When the controlled EC potential is tuned in a certain energy range, the technique is dynamic and known as voltammetry. Here, the resulting current, I_{EC}, flowing through the electrode is measured as a function of the applied EC potential, V_{EC}.

A traditional electrochemical set-up for voltammetry is the so-called three-electrode cell, shown in **Figure 5**.

3 It is the loss of electrons or an increase in the oxidation state by an atom, ion or molecule.

4 It is the gain of electrons or a decrease in the oxidation state by an atom, ion or molecule.

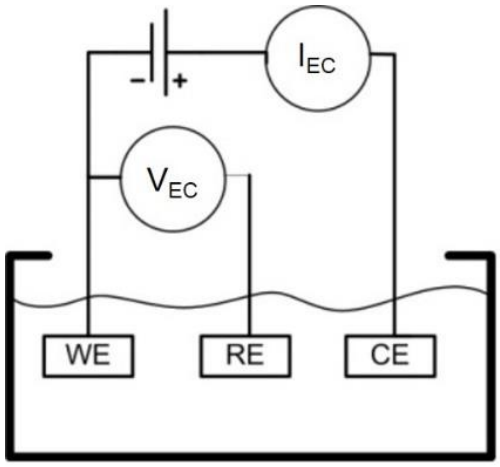

***Figure 5**. Schematic diagram of an electrochemical cell with three electrodes: working electrode (WE), reference electrode (RE) and counter electrode (CE).*

The three-electrode cell consists of a working electrode (WE), a reference electrode (RE), and an auxiliary (counter) electrode (CE). The surface oxidation (reduction) of interest takes place at the WE, while reduction (oxidation) occurs at the CE, for balancing the total charge of the system; the RE has a constant potential inside the electrochemical bath and ensures a good reference for the WE.

Working and counter electrodes are immersed directly in the electrolyte, whereas the RE is generally placed in a separate compartment (to avoid contamination) and connected to the cell via a salt bridge. The main criteria for an electrode to be classified as a RE are: i) to provide a reversible half-reaction, in which the electrode potential can be determined by the concentration of the half-reaction participants (by the Nernst equation) [49]; ii) to have a constant potential over time, i.e. to be an almost ideal non-polarisable electrode, so that its potential does not vary with the current passing; iii) being easy to be assembled and maintained. Many materials and configurations (not discussed here), which fulfill the above criteria, are used [50]. In all these cases, the RE potential is preferably referred to the standard hydrogen electrode (SHE), which can be

realized by a contact between molecular hydrogen and its ions on the surface of a platinum (Pt) wire. Here, the main reaction is the electron transfer between the neutral species (H_2) and the ions (H^+), as described by the following equation:

$$2H^+_{(aq)} + 2e^- \rightarrow H_{2(g)}$$

The EC potential of the reaction can be calculated from the Nernst equation:

$$E = \frac{RT}{F} ln \frac{a_{H^+}}{\sqrt{p_{H_2}/p_0}}$$

where a_{H^+} is the activity (effective concentration) of the hydrogen ions and p_{H_2} the gas pressure referred to atmosphere (p_0). At 25 °C, E = 4.43 V [51] but to be a term of comparison with all other electrode reactions, E is declared (convention) to be zero at all temperatures. A typical SHE design is shown schematically in **Figure 6**.

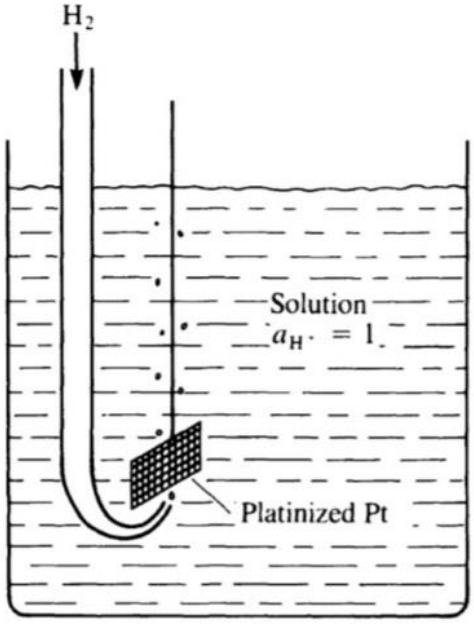

Figure 6. Scheme of the standard hydrogen electrode (SHE).

Unfortunately, SHE, as well as traditional RE (e.g. calomel and Ag/Ag chloride electrodes), have a limited range of applicability. With these electrodes the liquid junction is problematic and they cannot be used, either with wholly solid-state EC cells or for very high-temperature reactions. To overcome these problems, it was reported that a Pt wire, immersed inside an EC cell filled with different electrolytes, maintain a steady (within few mV) electrode potential [52]. Obviously, thermodynamic equilibrium cannot exist, since there is no common component (anion or cation) in the two adjacent phases (as H_2/H^+ in the SHE). To stress the differences with respect to a true RE, Pt wire is usually called a quasi-RE (QRef) [52]. Pt-QRef shows many advantages: it is very easy to be used; it shows a low impedance; it does not require a salt bridge; it does not contaminate the electrolyte solution; it is stable in many acids and does not disperse undesired ions in the EC solution.

For these reasons, I decided to use a Pt-QRef in all the reported experiments of this thesis. The Pt wire is immersed in the electrolyte solution for 24 h before each experiment and then inserted in the EC cell. The Pt-QRef shows a defined energy shift of + 0.740 V vs the SHE, when used in diluted H_2SO_4 electrolytes, in agreement with the literature [36]. A meaningless difference (few tens of mV) is observed with the other acid solutions used.

In voltammetry, an EC potential is applied to the WE with respect to the RE to alter the equilibrium conditions. In the presence of electroactive species (here, the diluted acid used as electrolyte solution) an ion diffusion (mass transport) from the bulk solution to the WE and CE starts. When ions are close to the

electrodes surface, they exchange electrons (redox process) and a faradaic current (I_{EC}) is measured between the WE and the CE[5]:

$$I_{EC} = nAFj$$

where F is the Faraday constant, n the number of electrons per molecule involved in the electrochemical process and A is the WE area [26]. Due to a diffusion process, the flux j is related to both the ion concentration (ϕ in mol/cm^3) and the diffusivity (D in cm^2/s [6]) at the interface, by the well-known Fick's law [53]:

$$j = -\nabla(D\phi)$$

The features observed in the voltammograms (I_{EC} vs V_{EC} plots) are thus related to the type of the ions in the electrolyte solution, the EC cell temperature, the number of exchanged electrons, the electrodes geometry, the timescale of the measurement, as well as to capacitive effects at the electrode/liquid interface, mass transport and surface phenomena that can be involved in the EC process.
This not simple picture is made even more difficult if other factors (e.g. the establishing of a local electric field, the ions migration, the presence of other charges, etc.), not contemplated in the Fick's law, are taken into consideration. Generally, these phenomena do not play a key role in voltammograms behavior and will be neglected in the following discussions [55].

[5] The faradaic current is measured on the WE, where half-reaction (oxidation or reduction, according to the applied EC potential) occurs.
[6] The diffusion coefficient (or diffusivity) in liquid is defined in first approximation by the Stokes-Einstein relation [54]:
$D = \frac{k_B T}{6\pi\eta r}$, where η is the dynamic viscosity (dependent from T) and r is the radius of the spheric ions.

2.1.2 CYCLIC VOLTAMMETRY (CV)

In cyclic voltammetry (CV), the EC potential applied to the WE is linearly swept starting from an initial value (V_{EC}^{i}) [26]. After reaching a switching potential (V_{EC}^{f}), the sweep is reversed and the potential returns to its initial value V_{EC}^{i}. A typical CV voltammogram is reported in **Figure 7**. According to the IUPAC convention, the positive potentials are plotted in the positive abscissa direction, thus the anodic currents (due to oxidation) are positive, while the cathodic currents (due to reduction) are negative. The presence of current peaks ($I_{p,a}$,$I_{p,c}$) at different EC potentials ($V_{p,a}$ and $V_{p,c}$, respectively) indicates that an electroactive couple is in the electrolyte solution. The main CV parameter is the potential scan rate ($\nu_{\text{scan rate}} = \Delta V_{EC}/t$), since it controls the timescale of the voltammetric experiment. Typical scan rate values range from 1 to 1000 mV/s, accordingly to the studied EC process [50]. In fact, driving the electron transfer at the electrode-electrolyte interface, the scan rate can influence the reversibility of the overall EC process, which is also influenced by the mass transport (see above). Consequently, if the scan rate is too fast with respect to the ion diffusion, the WE is polarized and an overpotential is required for the oxidation (or reduction) process. This alter the voltammograms, giving rise to unique CV profiles.

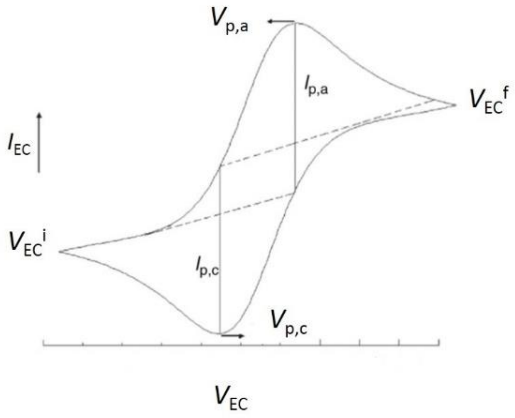

***Figure 7**. Cyclic voltammogram simulated for reversible charge transfer: Vp,c, cathodic peak potential; Vp,a, anodic peak potential; V_{EC}^{i}, initial potential; V_{EC}^{f}, switching potential; Ip,c, cathodic peak current; Ip,a, anodic peak current.*

In the case of a reversible process, the intensity of the faradic current, I_p (both anodic and cathodic), is a root-square function of the scan rate and the ratio $I_{p,a}/I_{p,c}$ is equal to 1[7]. The energy separation (ΔV_p) between the anodic and cathodic peaks, defined as $\Delta V_p = (V_{p,a} - V_{p,c})$, is relatively small and corresponds to a value of *ca.* $59/n$ mV (at 298 K) [45][8], regardless the used scan rate (as illustrated in **Figure 8***a*). If ΔV_p changes as a function of the scan rate, the redox process is irreversible (see panel *b*).

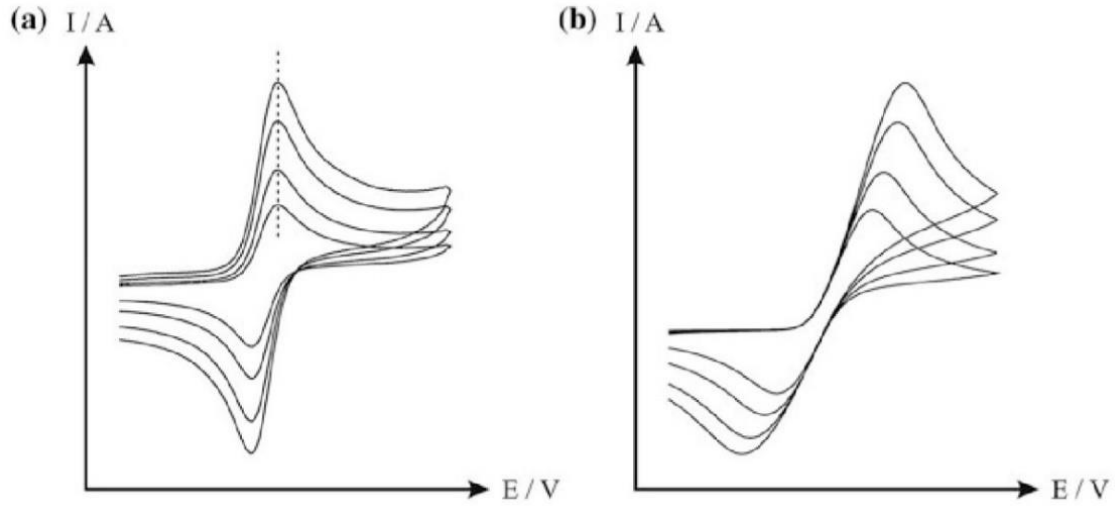

***Figure 8**. Reversible (**a**) and irreversible (**b**) CV responses. When the scan rate is enhanced, the peak maxima intensity increases (both in a and in b) and a potential shift occurs in the irreversible case (b).*

During the redox reaction, the total charge exchanged between solution and electrode can be evaluated from the acquired voltammograms. Traditionally, a

[7] The latter condition is not respected for irreversible process.

[8] Values greater than 59/n mV are indicative for an irreversible process.

linear background is subtracted from the anodic or cathodic peak (see Figure 7) and the subtended area is calculated. The latter is proportional to the exchanged charge, as clarified by the following equation:

$$A_{a(c)} = \int_{V_{EC,i}}^{V_{EC,f}} i(V)dV = v_{scan\ rate} \int_{t_i}^{t_f} i(t)dt = v_{scan\ rate} Q_{a(c)}$$

The anodic curve gives rise to the oxidation charge (Q_a), while the cathodic feature to the reductive Q_c. Similarly to what reported above, the ratio $Q_a/Q_c = 1$, if the electrochemical process is reversible ($Q_a/Q_c > 1$, for quasi-reversible or irreversible process) [56].

2.1.3 NORMAL PULSE VOLTAMMETRY (NPV)

As discussed above, CV is a diffused EC technique used to activate EC processes and to obtain information (reversible or irreversible processes and charge transfer) about the half-reaction (oxidation or reduction) occurring at the WE. Nonetheless, the continuous V_{EC} sweep activates the eleactroactive species in a series, without waiting the final stead state of the process, which usually takes few seconds. In addition, the faradaic current in CVs is influenced by both the charging and the discharging of a capacitive region at the electrode-electrolyte interface (Helmholtz layer, see **Figure 9**), caused by the presence of ions in front of the electrode surface [57].

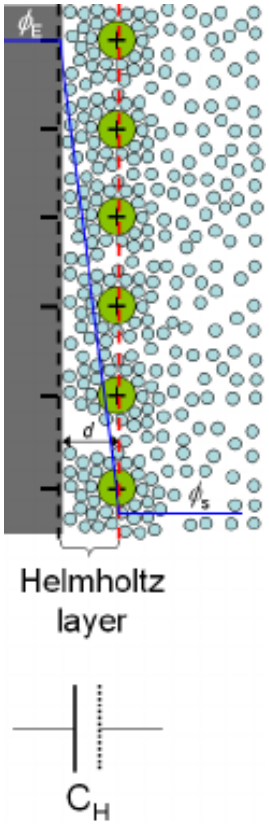

***Figure 9**. Helmholtz layer. The WE surface is negatively charged and cations (green spheres) are placed in front of the electrode. Solvent molecules (cyan small spheres) are interposed between the WE and the cations, giving an effective distance d between them. The geometrical parallel surfaces, where charges are orderly disposed (dashed black and red lines), can been thought in terms of capacitor armors (C_H). The linear behavior (in first approximation) of the potential (ϕ) at the electrode (E)-solution (S) interface is represented by the blue line.*

Charging currents, characteristic of dynamic EC techniques, have different behaviors with respect to faradaic currents because they do not require an electron transfer trough the electrode/electrolyte interface. In particular, charging and faradaic currents show different evolution as a function of time: the former have a fast exponential decay (few ms), while the latter show a $t^{-1/2}$ decay due to the slow ions diffusion in the bulk electrolyte (see above), as illustrated in **Figure 10**.

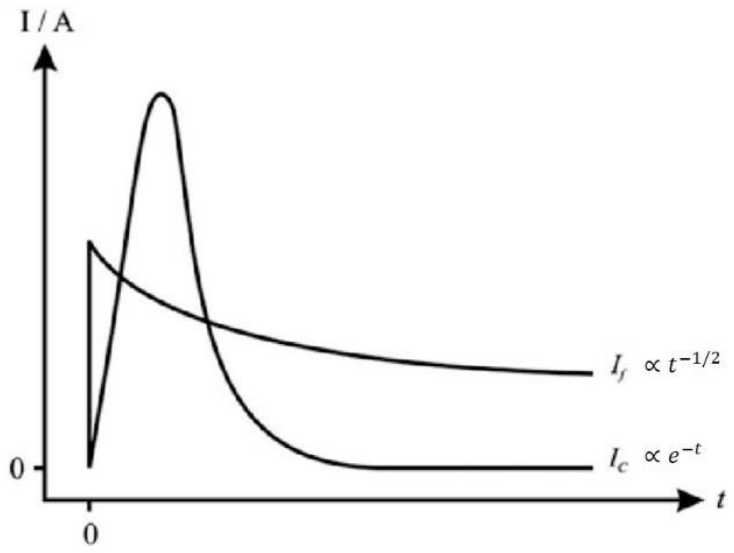

***Figure 10**. Comparison between capacitive and faradaic currents as a function of time.*

Accordingly, the EC current measurement closely corresponds to the faradaic counterpart after a time delay of few tens of milliseconds, being now negligible

the charging currents. This analysis is possible with the so-called normal pulse voltammetry (NPV) [26]. Here, a single or a series of regular voltage pulses (with a certain width and amplitude) is applied to the WE. The measured current is compared with the value acquired at a constant "baseline" voltage, where no EC processes occur (normal pulse[9]). It is important to note that, by setting a defined potential V_{EC} to the WE, the NPV activates only those chemical reactions whose EC potentials do not exceed V_{EC}. This allows singling out some EC processes from others (i.e. those occurring at higher potential with respect to V_{EC}) [58]. In this thesis, I deeply exploit this peculiarity of the NPV, in view of discriminating concomitant processes occurring during the ion intercalation in graphite.

To enhance the possibilities offered by NPV, some parameters have to be set appropriately. These can be collected as follows:

1) **Step Potential** (or pulse amplitude), which is the height (in V) of the potential pulse;
2) **Duration** (or pulse width), which is the time interval (in s) of the potential pulse. In this thesis, values ranging from 0.2 to 3.2 s (faradaic regime) are used;
3) **Sampling Interval**, which is defined as the time interval between two consecutive measurements of the I_{EC}. In this thesis, the sampling interval value is 1 ms.

[9] Differently, in differential pulse voltammetry (DPV) the series of regular voltage pulses is superimposed on the potential linear sweep, used for the traditional CV.

2.2 *SCANNING PROBE MICROSCOPY*

A commercial 5500 scanning probe microscope (SPM) from Keysight Technology was used in this experimental work. Two main configurations were adopted:

- scanning tunneling microscopy (STM);
- atomic force microscopy (AFM).

SPM techniques use raster scanning of the sample surface, done by a small dimension probe. The surface scanning is obtained by high-resolution piezoelectric actuators, which move the probe across the sample. For each (x, y) coordinate couple, the interaction (see below) between probe and sample is recorded as one data point. The collection of data points results in final SPM images. The latter were analyzed by Gwyddion free-software.
The 5500 system offers the possibility to combine the SPM techniques with a three-electrode cell. The sample analysis can be thus extended to the liquid environment, by using both the EC-STM and EC-AFM (see below for details).

2.2.1 (EC) STM. GENERAL DETAILS

The invention of the STM by Binning and Rohrer in 1982 [50,60] paved the way for the investigation of surfaces on the nanometer scale [61-64]. Before 1986, the STM was usually used for measurements in Ultra-High-Vacuum (UHV) or in air, but since Sonnenfeld and co-workers [65] demonstrated that STM can operate in deionized (type 1) water, much progress has been made to explore the potential of this technique to work at the solid/liquid interface [66,67]. The first

application of STM even in conductive solutions is attributed to K. Itaya, who developed the first electronic circuit (bi-potentiostat) to pilot the STM tip in an electrolyte (see below), realizing the first so-called EC-STM [68,69]. The latter combines the three-electrode cell with a STM scanner. It is payed specific attention to the metallic STM tip that, being biased to collect the tunneling current, represents a fourth electrode inside the EC cell. The bi-potentiostat is able to set the tip EC potential to a value where no redox process occur, so minimizing the faradic current flowing through the tip [70,71]. The V_{bias} between the tip and the WE sample is always obtained as a difference, but between the sample (WE) and the tip EC potentials. In view of helping the bi-potentiostat to minimize faradaic currents on the tip, the latter is usually covered by Apiezon wax. Only the very last apex of the tip is left uncovered to collect the tunneling current. In **Figure 11**, the working EC-STM set-up is illustrated.

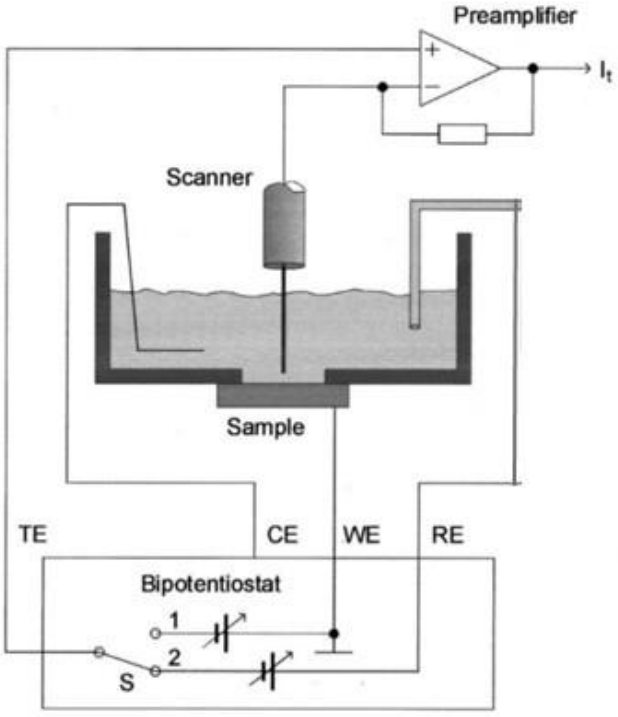

***Figure 11**. Principle of the potential control for potentiostatic and potentiodynamic imaging (TE = tip electrode) [70]*

In the last years, EC-STM has collected the interest of a very wide research community for the possibilities offered by different studies and applications, such as: i) surface corrosion [72,73]; film growth at the solid/liquid interface [75]; adsorption of molecules/ions [76,77]; imaging of redox species [78]; nano-catalysis [79]; ions intercalation [42,44]; etc. Despite the impressive results obtained by this technique, the offered possibilities are still boundless as declared by H. Rohrer in one of his last invited talk on the STM technique perspectives.

2.2.1.1 Fundamentals of STM

The real-space visualization of surfaces with an atomic-resolution is one of the most important characteristics of STM [18]. This is realized by measuring the tunneling current flowing between a sample (usually metal or semiconductor crystal) and a biased sharp conductive tip, placed at few Å from the sample surface. Tunneling is a quantum-mechanical phenomenon in which an electron, with an energy E, can penetrate a potential barrier $\Phi > E$. The wave function ψ, describing the quantum state of the electron, decays exponentially in the classically forbidden region according to:

$$\psi(z) = \psi(0) exp \frac{-z\sqrt{2m(\Phi - E)}}{\hbar}$$

where m is the mass of the electron, z is the barrier height and $\hbar$ is the Planck constant ($\hbar = 1.05 \times 10^{-34}\, Js$). When the STM tip approaches the sample surface, the electron wave functions of both the tip and the sample overlap within the insulating narrow barrier (e.g. vacuum, air, etc.). A tunneling current (I_T) flows between the tip and the sample as a function of the sign and value of the bias voltage applied to the tip, according to the following equation [80]:

$$I_T \propto \sum_{\mu\nu} f(E_\mu)[1 - f(E_\nu + \mathrm{eV}_{bias})] \times \left|M_{\mu\nu}\right|^2 \delta(E_\mu - E_\nu),$$

Here, f ($E_{\mu\,(\nu)}$) is the Fermi function of the probe (surface), V_{bias} is the applied bias voltage to the tip, $M_{\mu\nu}$ is the tunneling matrix element between state ψ_μ of the tip and state ψ_ν of the surface and E_μ is the energy of state $\psi_{\mu\,(\nu)}$ in absence of tunneling. According to the theoretical model proposed by Tersoff and Hamann [80] for the interpretation of the tunneling current, the latter is proportional to the surface local density of states (LDOS) at the Fermi level:

$$I_T \propto V_{bias}\, e^{-kz\sqrt{\varphi}}\, \rho(z\,, E_F).$$

where the quantity $(\Phi - E\ )$ is approximated by the working function φ and the LDOS is expressed by the function $\rho(z,E_F)$.

The tunneling current exponentially decreases as a function of the separation z between tip and sample, giving an extremely highly vertical resolution to the STM: a tip-sample distance enhancement of 1 Å produces a tunneling current reduction of about one order of magnitude.

The STM lateral resolution is also enhanced by the tunneling effect (see **Figure 12**). It is possible to demonstrate that an atomic separation down to 2 Å is easily resolved [81,82].

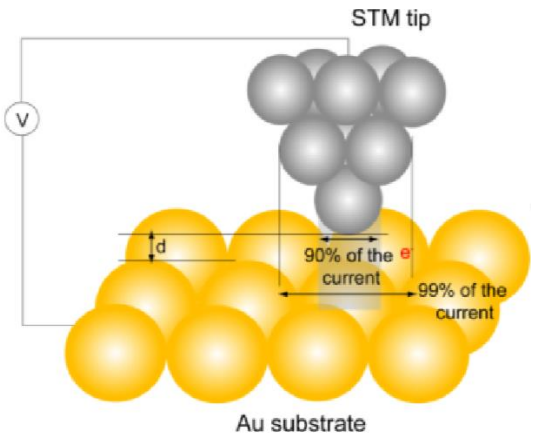

***Figure 12**. Schematic diagram of scanning tunneling microscopy depicts the tip sample interaction [82].*

The metal (W or Pt-Ir) tip is placed into the scanner, i.e. a piezo tube containing three transducers (P_x, P_y, P_z), which converts electric signals V_x, V_y, V_z (with an amplitude ranging from 1 mV to 1 kV) into a tip mechanical motion, in a wide length range (from sub-Å to µm) [83].

Two operating modes can be chosen for the STM signal acquisition, namely the constant current mode and the constant height mode [84].

Constant-current mode: I_T and V_{bias} values are kept constant. To this end, the voltage applied to the P_z piezo is governed by a current feedback system, which adjusts the tip-sample distance (z) to keep the I_T constant during the surface scanning (see representative scheme in **Figure 13**).

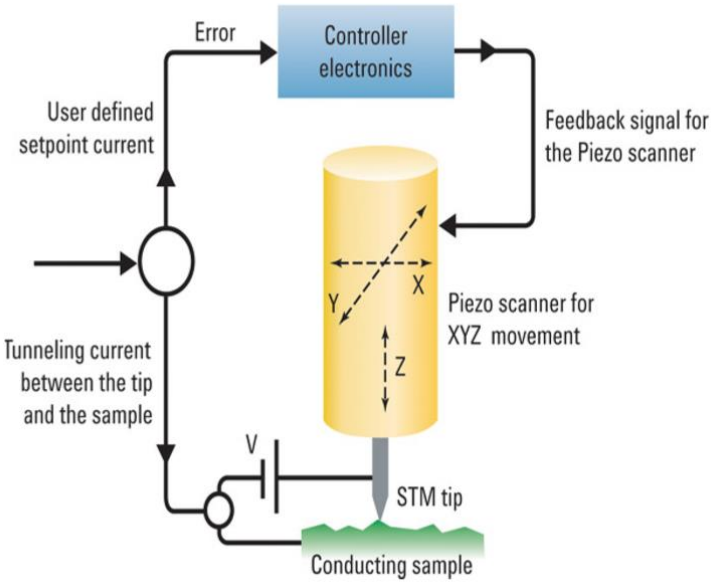

***Figure 13**. STM feedback system scheme.*

In this acquisition mode, large and rough sample areas can be, in principle, imaged without any damage of the tip or of the sample surface (tip crash phenomena). A drawback is instead the limited scan rate, which must be kept relatively slow allowing the feedback system to fine control the z position of the tip.

Constant-height mode: z and V_{bias} values are kept constant. A higher scan rate is allowed in this STM configuration and, hence, thermal drifts effecting a high resolution imaging can be largely eliminated. Conversely, being the feedback system switched off, scan sizes are limited and confined to flat areas in order to avoid "tip crash" phenomena [85].

2.2.2 (EC) AFM. GENERAL DETAILS

The main limitation of STM is that it cannot be used with insulating substrates. However, at the sort of distances where tunnelling currents occur, there is an attractive or repulsive force between atoms in both tip and substrate, which is independent of the conducting or non-conducting nature of the substrate. In order to measure this interaction force, Binnig, Quate and Gerber [19] developed the AFM set-up, in 1986. The AFM probe is a sharp tip, normally made of silicon, mounted on the end of a soft cantilever spring, whose changes are optically monitored by a laser beam deflection [86]. During the scanning of the surface, tip-sample interaction forces perturb the AFM spring and the consequent deflection is revealed by a photodiode detector. Since these forces can be electrostatic, frictional, capillary or magnetic, AFM is suitable for wide class of interactions [87].

The AFM lateral resolution is closely related to the tip radius (order of tens of nanometers) and, consequently, the technique is more suitable for a morphological characterization of the sample surface, rather than for its structural analysis. In principle, AFM can work in any kind of environment (vacuum, air and even liquid). The first application of AFM inside an EC cell dates back to 1996, when T. Kouzeki and co-workers studied the molecular assembling of naphtalocyanine at the solid-liquid interface [88]. Being not biased, the AFM tip does not play as a forth electrode in the EC cell, as conversely observed for the STM tip, and does not require any special electronics (bi-potentiostat) for the tip control in liquid. Constrains are instead imposed to the electrolyte solution that has to be transparent for the detection of the laser beam deflection. Despite this fact, EC-AFM has dominated researches on the solid-liquid interface [89,90]. In particular, EC-AFM can monitor the growth and

evolution of living cells and characterize their mechanical properties in real environments [91,92].

2.2.2.1 Fundamentals of AFM

The AFM tip-sample interaction is well described, in first approximation, by the empirical Lennard-Jones potential, which characterizes interatomic and intermolecular interactions. The Lennard-Jones (or 12 - 6) potential is described by the following equation:

$$V_{LJ} = \varepsilon \left[\left(\frac{r_m}{r} \right)^{12} - 2 \left(\frac{r_m}{r} \right)^{6} \right]$$

being ε the depth of the potential wall and r_m the distance at which the potential reaches its minimum (-ε) [93].

The resulting force shows the behavior, in function of the tip-sample atomic distance, reported in **Figure 14** [94].

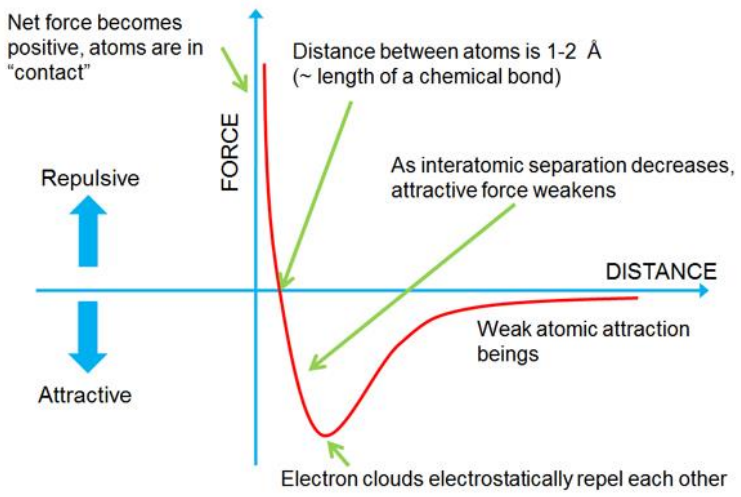

Figure 14*.Behavior of interaction forces, arising from the Lennard-Jones potential, as a function of the tip-sample distance. The different repulsive and attractive regimes are also indicated.*

The attractive region belongs to the weak long-range van der Waals interaction between dipoles, which follows a $1/r^6$ law. The repulsive region is instead dominated by a term $1/r^{12}$ that only acts below 1 - 2 Å (length of a chemical bond).

However, a full description of the tip-sample interaction should take into account specific short-range forces (adhesion/contact and capillarity forces) arising from the surface, which are not considered in the Lennard-Jones approximation. Adhesion/contact forces appear when two bodies, put into contact, undergo a deformation, which strictly depends on the elastic properties of the materials. The analytical relations between the applied force and the resulting deformation, expressed by the stress (σ) and strain (ε) tensors, can be obtained by using different theoretical models, which take into account (under several conditions) the surface energy contribution. According to different approximation degrees, the Bradley theory [95], the Derjaguin-Mfiller-Toporov (DMT) theory [96] and the Johnson-Kendall-Roberts (JKR) theory [97]have been developed in the past. Capillarity is instead an attractive force exercised by the liquid meniscus created in ambient condition between tip and sample; it follows from the adsorption of a thin water layer on a hydrophilic surface.

The tip-sample interaction plays a key role in the AFM imaging acquisition (or mode). The latter can be divided into static and dynamic modes [98].

In the static (contact) mode, the AFM tip approaches the sample at distances where the repulsive forces act (see Figure 14). The latter are then maintained constant. Conversely, in the dynamic (non-contact or tapping) mode, the cantilever oscillates and the AFM tip periodically reaches the surface at a distance where both attractive and repulsive forces act. This mode is preferred when samples are particularly fragile, such as molecules physisorbed on a substrate. Here, an AFM tip driven in contact configuration could remove and drag

molecules across the scanned area. The drawback is that non-contact mode shows a decreased lateral resolution compared to the contact mode.

The dynamic acquisition has two sub-acquisition methods: amplitude-modulation (AM) and frequency-modulation (FM). In AM-AFM, the scanner actuator is driven by defined potential amplitude (V_i) and frequency (f_i), close to the resonance frequency (f_0) of the cantilever. When the tip approaches the sample (in the repulsive force region), elastic and inelastic interactions change both V and f with respect to the driving signal of the cantilever (V_i and f_i). These changes are used as feedback signals. In FM-AFM, the feedback signal is instead represented by changes of the eigenfrequency f_0 of the cantilever, being affected by the attractive tip-sample interactions during the scanning.

A focused laser beam, pointing on the backside of the cantilever and reflected off it, detects the tip deflection during the surface scanning. A 4-quadrants photodiode detector records changes in the laser spot position, as reported in **Figure 15**. The laser spot movement is interpreted in terms of vertical deflection (AFM, changes between the 1-2 or 3-4 quadrants) and lateral friction (LFM, changes between 1-3 or 2-4 quadrants), being the overall intensity (SUM = 1+2+3+4) constant.

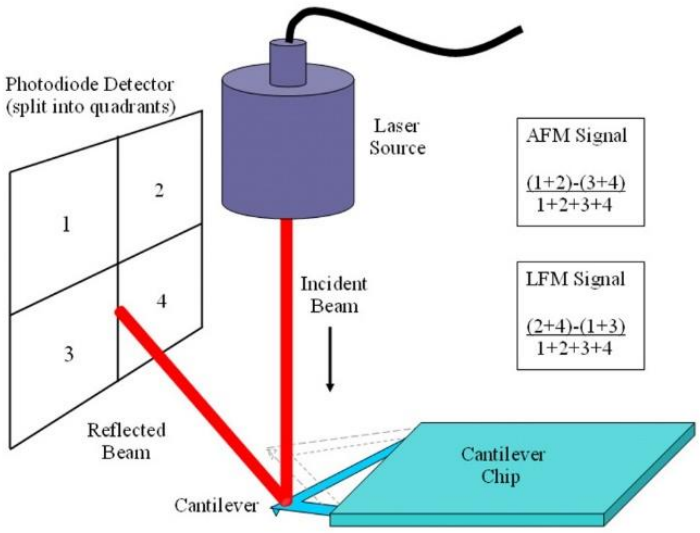

***Figure 15**. Photodiode detector operation. AFM, LFM and SUM signals are reported.*

The laser spot alignment on the photodetector is a user-friendly operation in vacuum or air condition. The alignment becomes more critical when the AFM cantilever is immersed in liquid. In this case, the change of the refractive index at the liquid/air interface causes an additional deflection of the laser spot path and a consequent photodiode adjustment is required. The cantilever material has to be chosen carefully to avoid matting of its surface in liquid and a consequent decreasing of the reflected laser light intensity. Finally, the SUM signal is affected by the electrolyte opacity (solute concentration), limiting the applicability of the EC-AFM to transparent (very diluted) solutions.

2.2.3 EC SET-UP FOR IN-SITU SPM MEASUREMENTS IN LIQUID ENVIRONMENTS

The three-electrode cell is made by a plastic material [polytetrafluoroethylene (PTFE)], which shows high resistance to corrosive chemical solvents (such as sulfuric, perchloric, phosphoric, hydrochloric acids, etc.), high melting temperature (about 300 °C), good mechanical resistance, easy handmade, low production costs, etc. [99]

An example of the EC cell used for the experiments reported in this thesis is illustrated in **Figure 16**.

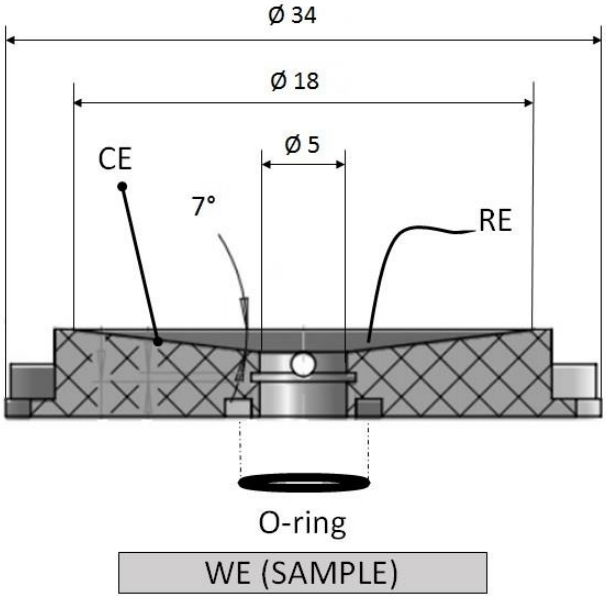

Figure 16. *Lateral section of one of the EC-cell (capacity of 600 μl) used for the STM experiments. The dimensions (diameter in mm and cell-grade in degree) are reported. The groove for the CE positioning is indicated. A Pt wire constitutes the RE, while the WE is represented by the sample. The 1 mm hole for tubing is visible in white in the center of the cell section.*

The Viton O-ring underneath the cell ensures the sealing of the electrolyte solution. Two clamps (not reported in the figure) press the cell on the sample (WE). Two 0.1 mm Pt wires are used as CE and RE (see the figure). In particular, trying to expose a comparable surface area with respect to the WE, the CE wire is bended to obtain a spring fully immersed in the electrolyte. Conversely, trying to minimize spurious currents on the RE, the latter just touches the electrolyte surface. A 1 mm hole is included in the cell scaffold (see the white circular section in Figure 16) for flow-through tubing. This orifice allows the continuous replacement of the electrolytic solution, when required.

In view of coupling the EC cell with both the STM and AFM scanners, a quite large window (Ø = 18 mm) is realized on the top of the cell. The EC cell volume is about 600 µl.

The EC cell and the sample are placed onto a sample-plate, prearranged with the electrical connections required for EC and scanning analysis (see **Figure 17)**, and mounted underneath the SPM scanner.

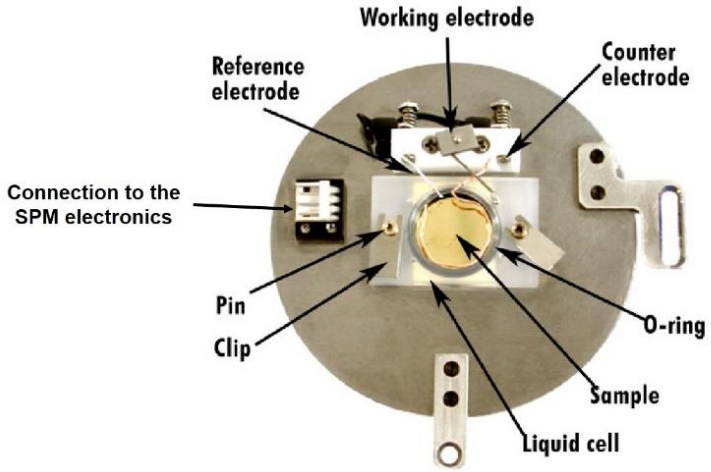

***Figure 17**. Photo of the EC cell used for EC-AFM, placed on the sample-plate.*

In this way, the STM and AFM scanners can be easily exchanged to acquire the electrode surface morphology and structure on different length scale, without perturbing the EC conditions. In addition, the 5500 SPM system provides a containment chamber, which can be filled with pure Ar, to avoid the electrolyte contamination from atmospheric oxygen or other gases.

2.2.4 EXPERIMENTAL DETAILS

A ZYH grade HOPG sample is used as WE; the size of the WE is quite large ($Ø_{EC\ cell} = 5$ mm) to simplify the EC cell clamping on the sample-plate. Before each experiment, the graphite crystal is exfoliated by an adhesive tape to gain a fresh and clean electrode surface. WE, CE and RE are then connected from the sample-plate to a low-noise bi-potentiostat/galvanostat (PicoStat) integrated in the SPM system.

Four kind of diluted acid solutions were prepared: 1 M[10] sulfuric (H_2SO_4), 2 M perchloric ($HClO_4$), 2 M phosphoric (H_3PO_4) and 2 M hydrochloric (HCl) acid. To name but a few, the preparation of 1 M H_2SO_4 electrolyte requires these values:

$$1 \text{ mol } H_2SO_4 = 98.1 \text{ g}$$

$$d_{(H_2SO_4)} = 1.840 \ {}^{g}/_{ml}$$

where the solvent density (d) is a physical property reported on the pure (99.99%) sulfuric acid package.

$$V_{\ (H_2SO_4\ in\ 1l)} = \frac{m(g)}{d\left({}^{g}/_{ml}\right)} = \frac{98.1\ g}{1.84\ {}^{g}/_{ml}} = 53.3\ ml$$

[10] The molarity (M) is a solute concentration expressed in number of moles of solute per liter of solution.

This means that if 53.3 ml of H_2SO_4 are put in (1000 - 53.3) ml of deionized (type 1) water, we obtain a 1 M diluted solution of H_2SO_4. Similar calculations allow obtaining the volume quantities of solute and solvent for the other three acid solutions used as electrolytes in the following EC measurements.

HCl and $HClO_4$ are strong acids that complete dissociate when diluted in water. The conjugated bases are Cl^- and ClO_4^-, respectively. H_2SO_4 is a strong acid for the first dissociation (HSO_4^-), while the concentration of SO_4^{2-} in water is immaterial. H_3PO_4 is not a strong acid and only the first dissociation can be considered ($H_2PO_4^-$). In the following table, I list both the pKa and the pH values of the used acids and the prepared solutions, respectively [100].

	conjugated base	pKa	M	pH
H_2SO_4	HSO_4^-	-3	1	0.0
$HClO_4$	ClO_4^-	-10	2	-0.3
H_3PO_4	$H_2PO_4^-$	2	2	0.9
HCl	Cl^-	-8	2	-0.3

***Table 1**. Important chemical parameters of the used diluted acid electrolytes.*

The chosen electrolyte concentrations (see above) are in agreement with preliminary graphite intercalation studies with the same solutions, reported in literature [101,102]. The diluted acids undergo a degasification process by bubbling Ar gas (5.5 grade pure) inside a separator funnel, for several hours before each experiment. Ar bubbling helps removing the dissolved and reactive atmospheric gases, such as oxygen and carbon dioxide, from the liquid. These

compounds alter the CV, NPV (spurious features) and SPM (precipitates) acquisitions.

The electrolyte purification and stability was tested by a preliminary CV. The scan rate (25 or 100 mV/s) is chosen to observe quasi-reversible electrochemical process on the WE (see above). After many (order of 100) CVs, no sign of neither contamination (i.e. strong slope of the faradaic currents) nor instability (i.e. EC potential shifts) have been observed. As a consequence, the atmospheric contamination of the previous purified electrolyte takes a long interval (more than 3 hours) with respect to the SPM acquisition time (order of few minutes). For this reason, all the experiments reported in this thesis were conducted in air, without the containment chamber.

A Pt/Ir wire, with 0.25 mm diameter and covered by Apiezon wax, was used as EC-STM tip. Antimony n-doped silicon tip (elasticity constant $k = 5$ N/m; cantilever length = 450 μm) was used for the EC-AFM acquisition. The cantilever is back-covered by reflective Al coating suitable for in liquid measurements. The tip radius is about 10 nm, resulting in a scan lateral resolution of about 100 nm.

Finally, all the AFM images reported in this thesis are acquired in contact mode.

3 EXPERIMENTAL RESULTS

3.1 *HOPG SURFACE IN DILUTED ACID SOLUTIONS BEFORE THE ELECTROCHEMICAL OXIDATION*

When HOPG WE was immersed in the cell, the EC potential was initially set at a value (0.3 V vs PtQRef) where no redox processes (null faradaic current) occur, regardless the diluted acid solution used as electrolyte. Being null the faradaic current, the HOPG basal plane remains stable in the liquid environment, as well as in air, for hours. As an example, **Figure 18** shows the HOPG surface morphology in H_2SO_4 solution.

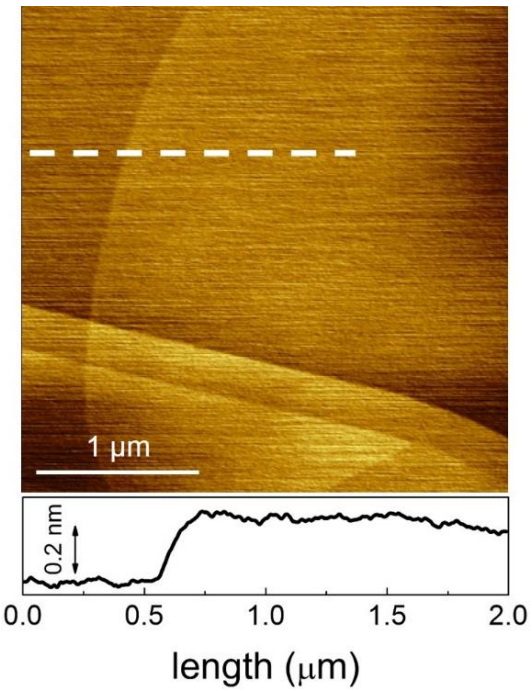

***Figure 18**. EC-AFM topography (3 x 3 μm^2) of the HOPG surface in 1 M H_2SO_4 at a WE potential = 0.3 V vs PtQRef. At the bottom, profile of a mono-atomic step. The white dashed line represents the profile cross section.*

Despite some stripes affecting the image in the scanning direction of the tip, as sometimes observed in the used electrolytes, the image reveals flat terraces, separated by mono- and multi-atomic steps. The profile (bottom panel), acquired along the dashed white line, reveals a step with an height of (0.30 ± 0.05) nm, which is compatible with a mono-atomic step, according to the graphite structure values reported in literature (see the Introduction). The terrace corrugation acquired along the profile is about 0.1 nm, in agreement with the surface corrugation observed and measured on a HOPG in air (see **Figure 19**).

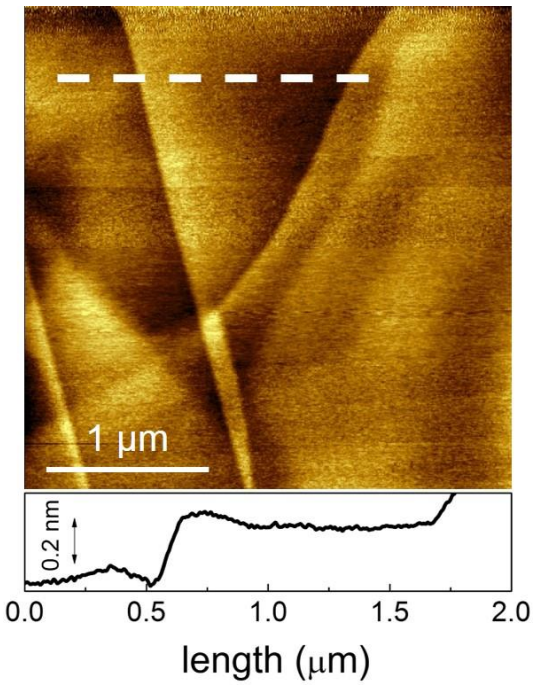

Figure 19. AFM topography (3 x 3 μm^2) of the HOPG acquired in air. At the bottom, the profile of a monoatomic step. The white dashed line represents the profile cross section.

The comparison between the HOPG surface morphology in liquid and in air allows an estimation of the EC-AFM resolution. The electrolyte does not affect the vertical sensitivity of the tip: the step height and the terrace corrugation are comparable in Figures 18 and 19. By considering both the lateral distance between the up and downstream of the step and the tip diameter, the lateral resolution is estimated to be not minor than 100 nm.

The HOPG surface structure was revealed by EC-STM on the same sample, by a simply replacement of the AFM with the STM scanner above the EC cell. The blow-up in **Figure 20** shows a centered hexagonal lattice, as expected in unperturbed graphite. The central carbon atom belongs to the honeycomb structure of the shifted underneath plane (see the Introduction). The atomic reticular path [(2.2 $\pm$ 0.3) Å] and the surface corrugation [(0.45 $\pm$ 0.08) Å, acquired along the dashed white line] are in very good agreement with previous EC-STM measurements reported in the literature [103].

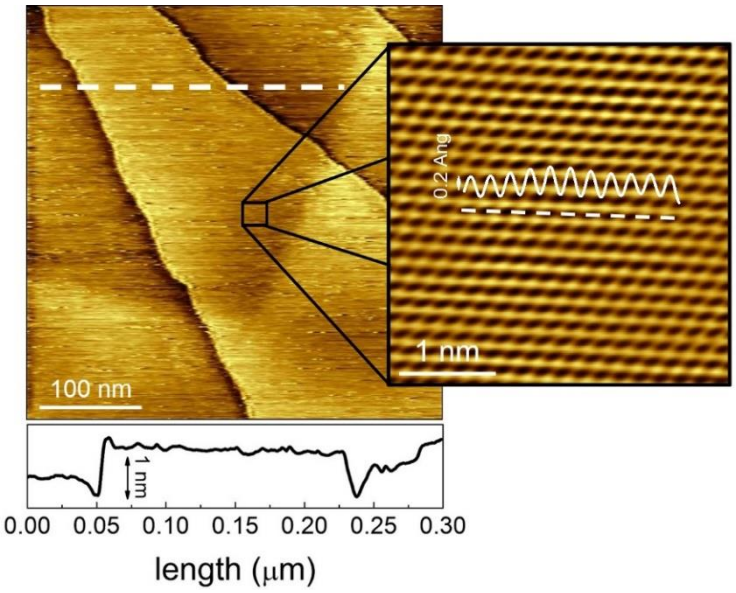

***Figure 20**. EC-STM image (400 x 400 nm^2) of the topography of a stepped region of the HOPG surface in 1 M H_2SO_4. V_{bias} = 0.3 V vs PtQRef; IEC = 0.7 nA. A zoom on the top of a terrace shows the centered hexagonal atomic lattice.*

3.2 *HOPG OXIDATION IN DILUTED ACID ELECTROLYTES BELONGING TO THE CLASS 2: 1 M H_2SO_4*

The electrochemical behavior of HOPG in H_2SO_4 was first examined by a traditional CV (single sweep) to find the EC potentials of the characteristic intercalation anodic peaks [38]. In **Figure 21**, the voltammogram in the 0.3 V ÷ 1.3 V is reported. The upper limit (1.3 V) was set to protect the EC-SPM electronic apparatus, avoiding that too intense faradaic current flowing through the WE could saturate the amperometer (I_{max} = 1 mA).

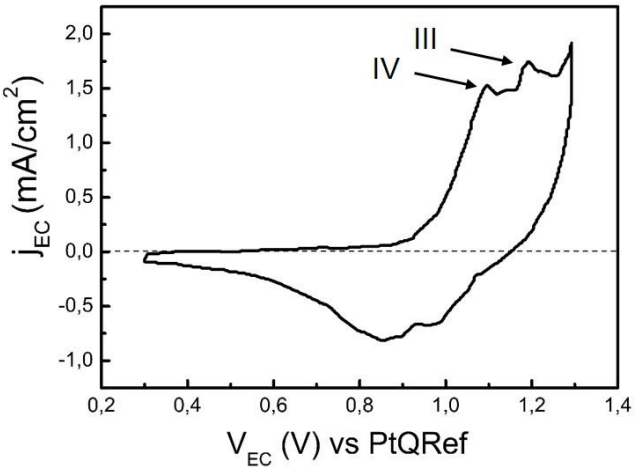

***Figure 21**. CV ($v_{scan\ rate}$ = 25 mV/s) in the EC potential range of 0.3 V ÷ 1.3 V vs PtQRef. The two stages of GIC (III and IV) are labeled in the voltammogram.*

Considering the voltammogram, three main EC potential intervals can be roughly distinguished: 1) the almost null current interval (between 0.3 and 0.9 V); 2) the onset window (between 0.9 and 1.1 V), where the measured current

rapidly increases; 3) the sulfate anion (HSO_4^-) intercalation interval (above 1.1 V). Here, two anodic peaks are observed at 1.1 and 1.2 V, which are labeled as IV and III GIC stages, respectively, in agreement with the literature [36].

During the cathodic sweep, negative currents, measured between 1.1 and 0.7 V, are usually interpreted in terms of a partial de-intercalation processes. The observed features change their energy position and intensity as a function of the last activated intercalation stage [104].

The evaluation of the overall anodic (Q_A) and cathodic (Q_c) exchanged charge requires a careful background subtraction, as discussed in the Experimental techniques paragraph. Being close to the oxygen evolution reaction (bubbling electrolyte above 1.3 V), the faradic current is very high and prevents an easy evaluation of the background. Trying to minimize possible sources of errors, I preferred to directly collect the j_{EC} as a function of time (see **Figure 22**). Here, the background (null faradaic current) is a simple horizontal line and the subtended area (with sign) represents Q_A or Q_C.

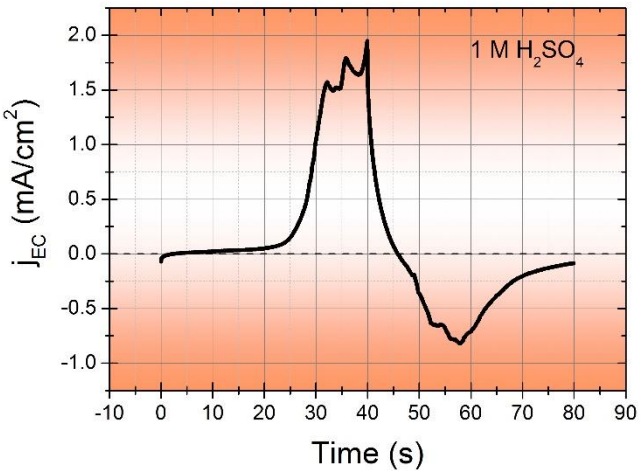

Figure 22. j_{EC} vs Time curve.

Normalizing for the exposed WE area, the anion concentration Q_A = (21.60 ± 0.02) mC/cm^2, while the cathodic concentration Q_C = (12.70 ± 0.02) mC/cm^2. The ratio Q_A/Q_C = 1.7 (> 1) indicates that the intercalation process in not reversible: part of the intercalated anions remain buried in the HOPG crystal. Some electrolytes (e.g. H_3PO_4, see below) show a clear anodic peak but an immaterial cathodic signal. In these cases, the ratio $Q_A/Q_C \rightarrow \infty$ and the chemical reaction is definitively irreversible. To stress such differences, we refer to the H_2SO_4 intercalation as a quasi-reversible process [105].

After anion intercalation, the HOPG surface morphology was investigated *in-situ* by EC-AFM, keeping the EC potential at 0.3 V.

In **Figure 23**, blisters clearly swell the basal plane of the pristine HOPG. The blister distribution above the whole graphite surface is not easy to estimate. I acquired many images (not reported here) from different parts of the sample. Few areas show blisters well separated one from the others. Conversely, some regions are covered by clusters of blisters, from which is not easy to extrapolate the number of assembled bubbles. Assuming the current density as uniform on the WE surface, differences in the local density of steps and defects could affect the final blister distribution. From these considerations, I calculate that at least 75% of the WE surface is swelled and affected by blisters. Consequently, Figure 23 is a well representative image of the mean HOPG morphology after anion intercalation. An analysis on many blisters (30 - 40) reveals that their lateral size covers a wide range, from 0.5 to 1 μm, while the height is about 20 nm.

A closer inspection was possible by acquiring the surface structure on top of a blister, by the EC-STM (inset in Figure 23).

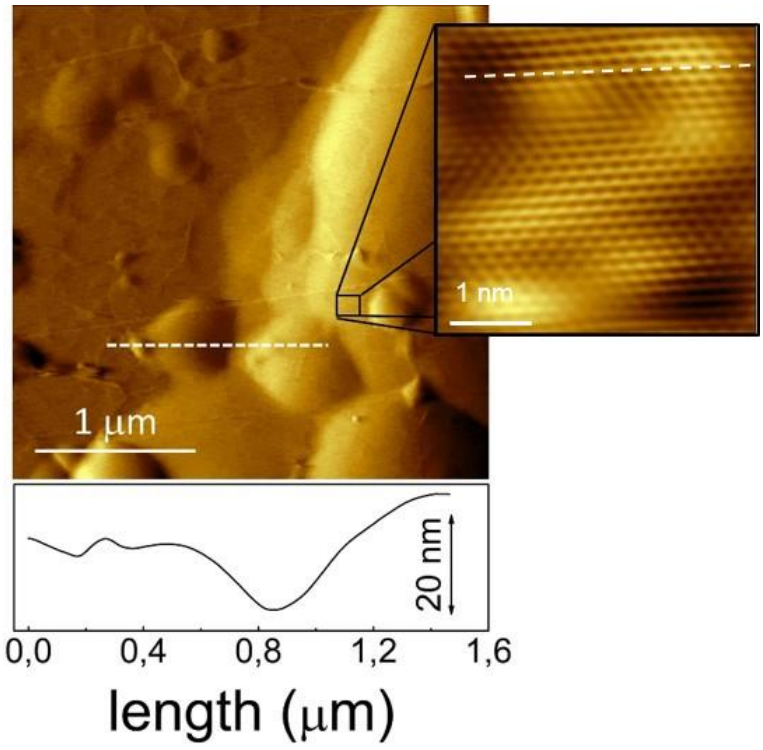

Figure 23. *EC-AFM topography image (3 x 3 μm^2). At the bottom, profile scan across the blisters. (Inset) Atomic resolution acquired on the top of a blister by the EC-STM (4 x 4 nm^2). The graphite lattice is clearly recognizable and the atomic corrugation well characterized along the reported profile. Local enhancement of the tunneling current reveals very small (nano-) protrusions (I_{tunnel} = 0.7 nA; V_{bias} = 0.5 V)].*

In the blow-up of Figure 23, it is possible revealing the atomic structure of graphite, acquired on the top of a blister. Interestingly, atoms do not lie on a flat plane: a local enhancement of the tunneling current reveals small (nano) protrusions [42,44], which show a mean lateral size of about 1.5 nm and a height of 0.12 nm. Nano-protrusions are not an electronic effect due to anion intercalation below the graphite surface, but a real topographic swelling of the uppermost graphite layers. In fact, several images acquired on the same scanned area (not reported here), but at different tip bias (tuned over about 700 mV), showed the same nano-protrusions (size, height and position).

An in-depth investigation of nano-protrusions revealed interesting features about their structure. In **Figure 24**, the swelled hexagonal geometry is analyzed by comparing the scan profiles (bottom panel) acquired along the protrusion edge (black dashed line) and across the nano-protrusion (red dashed line). From a geometrical evaluation, the C-C-bond length is stretched by about 3%, as calculated by the reported data (bottom panel). This value is not negligible for graphite surface but it is admissible in graphene sheets, as deduced from its mechanical properties [106-108]. Interestingly, I observe that these nano-protrusions recall comparable structures (called nano-bubbles) recently observed on the graphene/Ir(100) interface, when sub-monolayers of Ar are intercalated inside the sample under vacuum conditions [109].

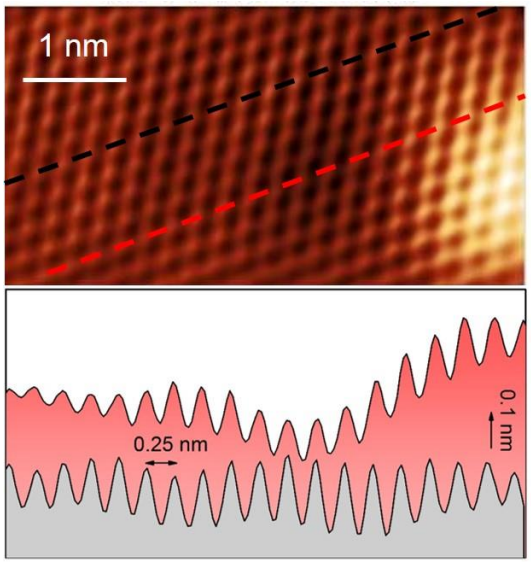

***Figure 24**. EC-STM topography of nano-protrusions (I_{tunnel} = 0.7 nA, V_{bias} = 0.3 V). At the bottom, two profiles are reported, in correspondence of the two dashed lines: the red one is across the nano-protusion and the black one is along the flat area. The reticular path of graphite is clearly discernible in both the profiles.*

Blisters and nano-protrusions are mechanically stable as a function of time, even if the intercalated HOPG sample is extracted from the EC cell and dried under a

gentle stream of pure nitrogen. The penetration of these features perpendicularly to the surface (z direction) is still under debate. Probably, blisters also affect buried graphite layers but nano-protrusions seem to be a surface-related characteristic.

Finally, I did not reveal significant morphological or structural changes if the CV is extended to a $V_{EC,f} \neq 1.3$ V (e.g. $V_{EC,f} = 1.1$ V). As soon as the IV intercalation stage is reached by a single CV sweep, both the EC-AFM and EC-STM reveal blisters and nano-protrusions, respectively.

3.3 *HOPG OXIDATION IN DILUTED ACID ELECTROLYTES BELONGING TO THE CLASS 2: 2 M $HClO_4$*

In close analogy with the experiments in sulfuric acid, anion intercalation peaks were observed by CV in $HClO_4$, too. In particular, three GIC stages (II, III, IV) can be produced if the EC potential is swept until 1.3 V [43]. Nonetheless, surface blistering was observed since the first (IV) GIC stage by EC-AFM [44]. In **Figure 25**, the CV in the potential range 0.3V ÷ 0. 95 V is reported.

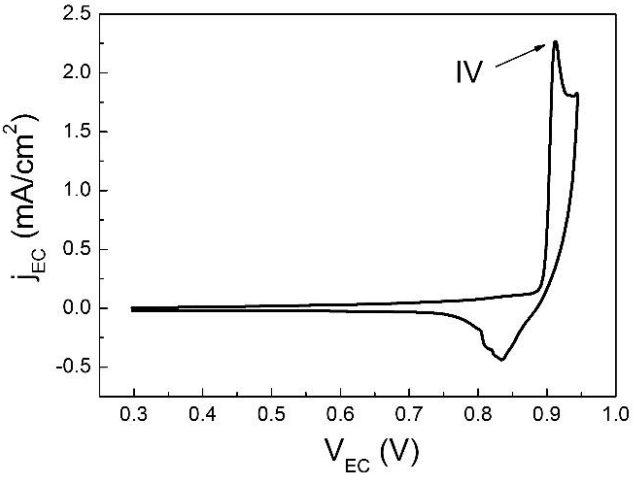

***Figure 25**. CV acquired between 0.3 and 0.95 V ($v_{scan\ rate}$ = 10 mV/s). The IV GIC stage is indicated in correspondence of the anodic intercalation peak at 0.91 V.*

Approximatively, the low-current interval lies between 0.3 and 0.88 V, the enhancement current onset window between 0.88 and 0.9 V and the perchlorate (ClO_4^-) anion intercalation interval between 0.9 and 0.95 V. The sharp anodic peak at 0.91 V corresponds to the IV GIC stage, while the broader negative structure represents the de-intercalation process, during the cathodic sweep.

Showing a huge slope, the evaluation of the whole exchanged charge (Q_A, Q_C) is easier obtained from the j_{EC} vs time curve (reported in **Figure 26**), in close analogy with the H_2SO_4 analysis.

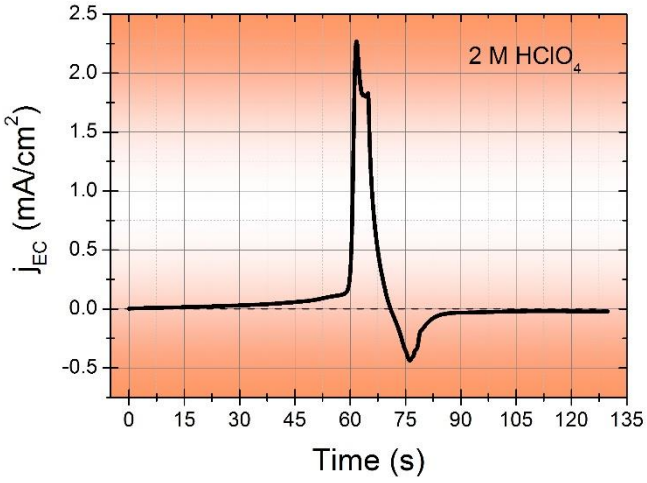

Figure 26. j_{EC} *vs time curve obtained from the voltammogram in Figure 25.*

The concentration of the anodic and cathodic charges are $Q_A = (14.10 \pm 0.05)$ mC/cm^2 and $Q_C = (3.88 \pm 0.05)$ mC/cm^2, respectively. $Q_A/Q_C \approx 3.6 >> 1$ and proves that this process is irreversible. If compared with the previous results in H_2SO_4, I can speculate that the amount of solvated ClO_4^- stored inside the graphite is double with respect to the solvated HSO_4^- anions.

After a single CV sweep, the surface morphology is analyzed by the EC-AFM (**Figure 27**). In the image, HOPG is swelled and some blisters affect the surface, in close agreement with previous results acquired on graphite in H_2SO_4 electrolyte. The error signal image (obtained from the difference between the set-point and the actual measured value, panel *i*) enhances the contrasts and helps

in distinguishing different blisters assembled in clusters. I did not find a significant difference in the distribution and sizes between blisters produced by class 2 acid electrolytes, suggesting a common mechanism of blister growth, as proposed by Murray and co-workers (see the Introduction) [40]. In fact, the profile, drown across a blister (bottom panel), shows sizes comparable to blister dimensions observed in the sulfuric electrolyte.

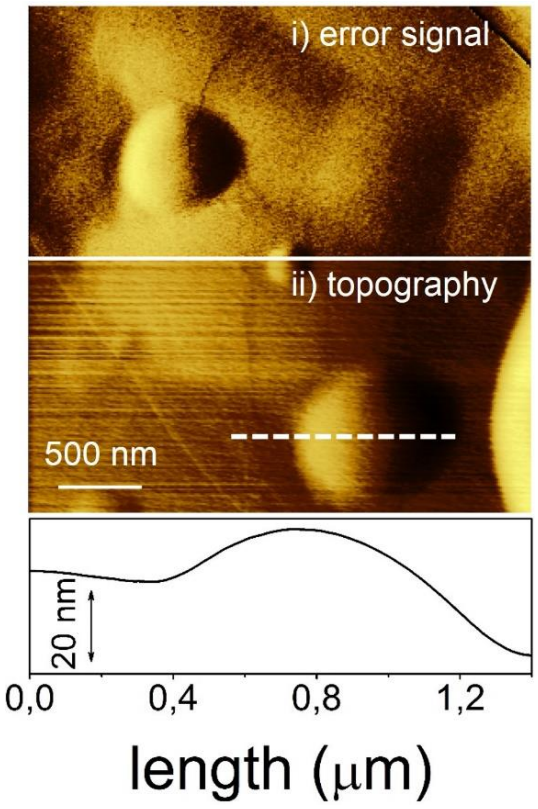

***Figure 27**. AFM image (3 x 3 μm^2). i) error signal and ii) topography of the HOPG surface after the IV stage of intercalation at 0.91 V. The EC potential was set at 0.3 V during the acquisition in liquid. At the bottom, the profile (white dashed line) across a blister is reported.*

Trying to disclose the very early phases of HOPG modifications during anion intercalation, morphological/structural surface changes occurring at the IV

intercalation stage were studied by a parallel CV and EC-STM acquisition. To this end, the EC-STM imaging was synchronized with a CV half-cycle, as reported in **Figure 28**.

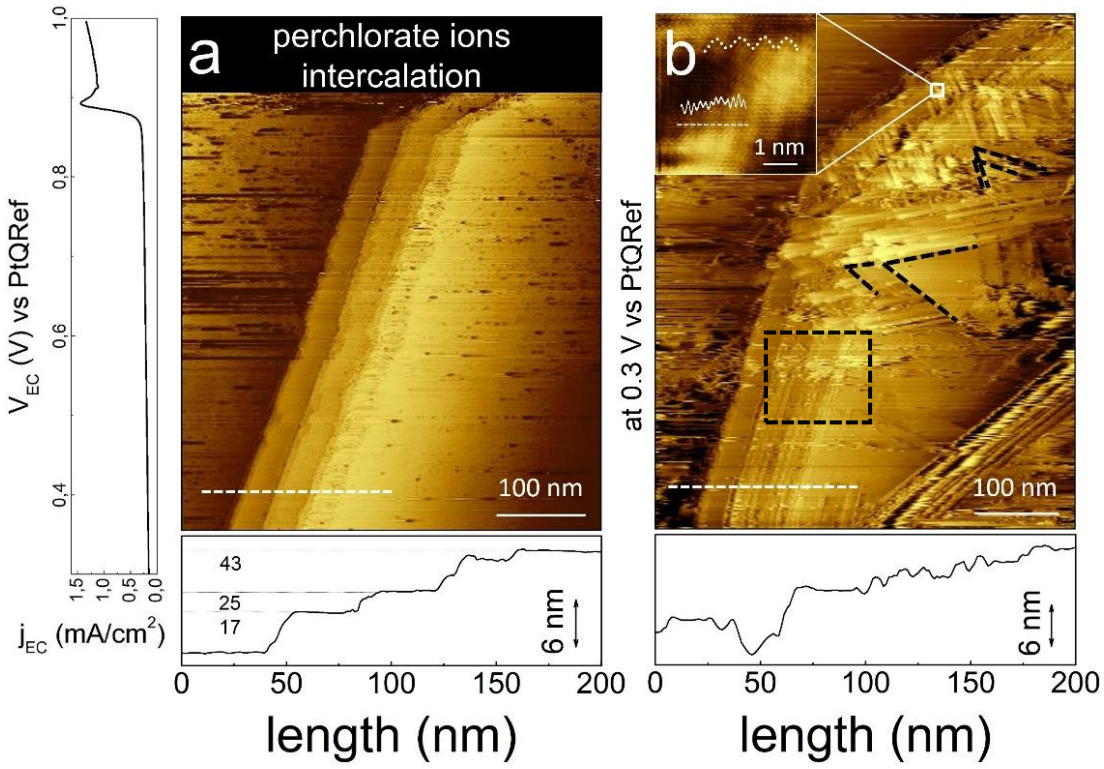

***Figure 28**. (a) EC-STM image (450 x 600 nm^2, I_{tunnel} = 0.2 nA) acquired on graphite immersed in $HClO_4$ solution. At the bottom, height profile of the graphite multi-atomic steps (17, 25, and 43 mono-atomic graphite layers) is reported. On the left, the CV half-voltammogram acquired during the EC-STM scanning (see text for details). The "perchlorate ion intercalation" region, in correspondence of the tip lifting off the surface, takes a few seconds to be covered during completion of the EC sweeping. The height profile taken along the dotted white line (bottom) shows flat terraces and sharp edges. (b) EC-STM image (450 x 600 nm^2, I_{tunnel} = 0.2 nA; V_{bias} = 0.3 V) acquired after anion intercalation at fixed V_{EC} = 0.3 V. Terrace and step erosions are marked with black dashed lines. At the bottom, scan profile of graphite terraces, along which a significant increase in surface corrugation is observed. (Inset) Atomic resolution obtained on nano-protrusions.*

In panel *a*, the positive WE potential sweeping started few seconds before the EC-STM acquisition. The latter started at the bottom line of the image as soon as V_{EC} = 0.35 V is reached. The EC-STM scan speed was tuned according to the CV

$v_{scan\ rate}$ (10 mV/s) so that each horizontal scan line refers to a specific V_{EC} value in the CV half-cycle (reported on the left side). At 0.9 V, the STM tip was gentle lifted off the surface to avoid scanning instabilities or tip-crashing with the electrode surface. In fact, the fast I_{EC} enhancement on the WE perturbs the measured tunneling current and the STM feedback control hardly follows these kind of changes. Nonetheless, the almost unperturbed surface morphology, observed before the "perchlorate ion intercalation" phase, suggests a negligible role of the solvated ClO_4^- at EC potentials below 0.9 V.

When the CV half-cycle is completed at 1.0 V, the sample potential was instantly set to V_{EC} = 0.3 V to reduce the faradaic currents, stabilize the STM current feedback and give the possibility of acquiring a second image on the same scanned area. Starting from the first horizontal line on the top of Figure 28 *b*, the STM tip revealed a HOPG surface morphology strongly affected by the intercalation process. Terraces are eroded due to the carbon dissolution at high EC potentials, resulting in a faceting process that damages the surface. New edges (indicated by the black dashed square) and vertices with preferential angles of about 60° (see the black dashed lines) are visible on the image. In accordance, the scan profile (reported at the bottom of the panel *b*) reveals a significant enhancement of the surface corrugation (4 nm) with respect to the pristine HOPG (0.1 nm).

Similarly to what observed after the anion intercalation in the H_2SO_4/HOPG system, nano-blisters are revealed in the image (see the panel *b* inset). The atomic resolution (white line) is modulated by a super-structure (dotted white line, lattice parameter = 0.5 nm), ascribable to a moiré pattern resulting from the anion intercalation, which partially lifts up the uppermost graphite layers from the deeper ones [110].

3.4 *HOPG OXIDATION IN DILUTED ACID ELECTROLYTES BELONGING TO THE CLASS 1: 2 M H_3PO_4*

Figure 29 shows the acquired single sweep-CV (continuous black line) in the 0.3 V ÷ 1.6 V EC potential range, where a clear anodic peak appears. The used scan rate was 150 mV/s, in agreement with values reported in the literature [114]. 0.3 V ÷ 1.1 V represents the low-current interval, the current enhancement onset lies in the 1.1 V ÷ 1.4 V window, while the 1.4 V ÷ 1.6 V interval represents the oxidation phase.

Here, in strong contrast with previous results acquired on class 2 electrolytes, where anodic features are always visible during consecutive CVs, the 1.48 V-peak disappears as soon as a second voltammogram is registered in the same EC potential range (dashed curve), suggesting a different EC process during the HOPG oxidation in diluted phosphoric electrolyte. In addition, the absence of a clearly coupled cathodic peak indicates that oxidation is completely irreversible. Despite this fact, the exchanged charge (Q_A) can be evaluated from the j_{EC} vs time plot, as reported in the **Figure 30**.

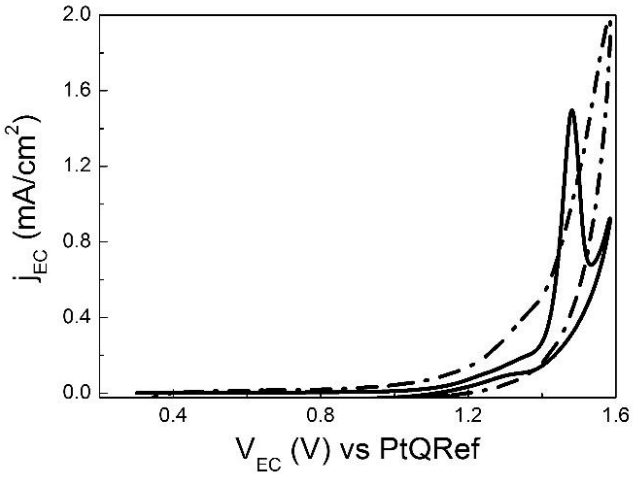

Figure 29. *Cyclic voltammograms ($v_{scan\ rate}$ = 150 mV/s) in the 0.3 ÷ 1.6 V range. The first EC sweep is indicated by the continuous black line, while the second cycle by the dashed line. Here, no clear anodic features are measured.*

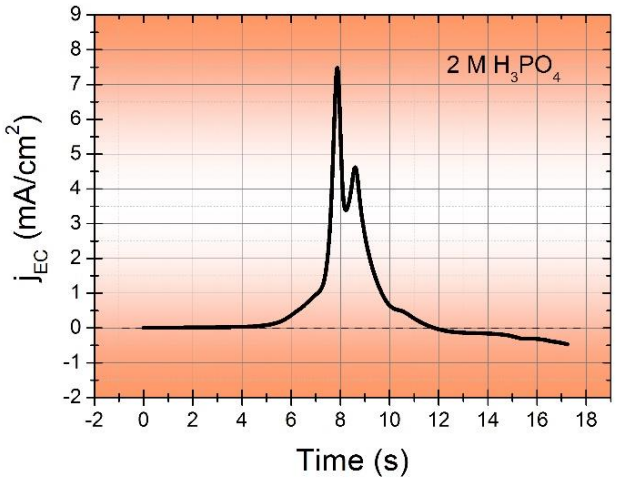

Figure 30. *j_{EC} vs time curve obtained from the voltammogram in Figure 29. Q_A = (50.31 ± 0.05) mC/cm^2. The cathodic feature is immaterial.*

EC-AFM also revealed noticeable differences in the surface morphology, after a single CV scan, with respect to what previously observed in class 2 electrolytes. Step edges are smoothed out and a negligible surface faceting is visible in **Figure 31**, ruling out massive carbon dissolution during the CV. Blisters are rare or completely absent in micrometer-square areas, suggesting that solvated anion intercalation and gases production are not the main process in this EC potential interval [112]. On the other hand, surface corrugation along the dashed white line is ten times larger than in pristine HOPG and comparable with respect to the graphite intercalated by class 2 electrolytes (see above).

Interestingly, EC-STM images were hardly collected after HOPG oxidation: I met with difficulties in tip approaching and scanning stabilization. This surface

evolution is compatible with the hypothesis that a thick and rough layer of adsorbates[11] contaminated the pristine HOPG. An *ex-situ* Raman investigation (reported in Ref. 113) confirms this picture: a highly modified and disordered graphitic layer coexists with some area of unperturbed graphite crystal. An in-depth analysis of this rough layer is beyond the main target of this work, focused on the mechanisms involved during the class 2 anion intercalation. Despite this fact, a chemical investigation of the deposited layer deserves further studies. In fact, nowadays, effects of phosphoric acid on graphite are only related to: i) corrosion, if diluted electrolytes are used [111], or ii) intercalation in pure solutions (85%); while, far in the past, the production of an insoluble black compound (called *fosfomellogeno*) was reported, after several hours of graphite activity as WE in diluted phosphoric electrolyte [114]. I incidentally speculate that the blackish film observed on my oxidized HOPG electrode (CV single sweep) by a simple optical investigation, and reported in Ref. 113, could be considered as the first stage of the *fosfomellogeno* growth on the graphite electrode.

[11] The adsorbate layer reduces the surface conductivity, perturbing the STM tip approach and scanning acquisition.

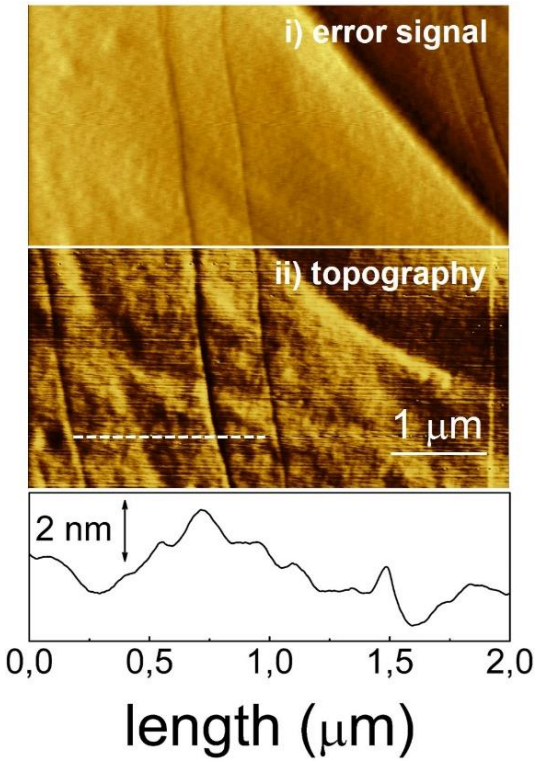

***Figure 31**. EC-AFM image (5 x 5 μm^2). i) error signal and ii) topography of the HOPG surface after a single CV sweep in 2 M H_3PO_4. The profile, represented by the dashed white line, is reported at the bottom.*

3.5 *HOPG OXIDATION IN DILUTED ACID ELECTROLYTES BELONGING TO THE CLASS 1: 2 M HCL*

A single sweep CV, in the -1.8 V ÷ 0.6 V energy range is reported in **Figure 32**.

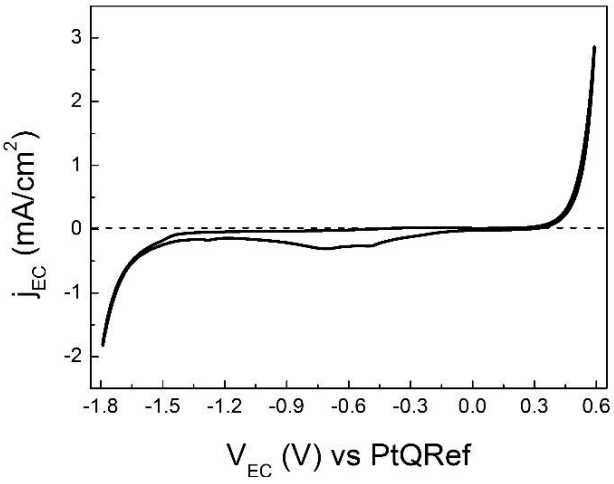

***Figure 32**. Characteristic CV ($v_{scan\ rate}$ = 100 mV/s) of HOPG in the HCl (2 M) electrolyte, acquired in the wide energy range between the hydrogen (-1.8 V) and the oxygen evolution reaction (0.6 V).*

Here, I extended the voltammogram towards a wider energy window to show that no anodic neither cathodic peaks are detected, apart small features between -0.9 V and -0.3 V, ascribable to a meaningless cathodic current, and expected when the EC potential is driven towards the oxygen evolution reaction (bubbling electrolyte above 0.6 V).

The EC-AFM image, reported in **Figure 33**, was acquired after the CV and with the WE potential kept at 0.3 V. The surface morphology is comparable to the

topography observed on graphite simply immersed inside an electrolyte, where no EC process was activated (see Figure 20). Sharp step edges, wide terraces, no graphite basal plane swelling and a surface corrugation (along the dashed white line) of about 0.1 nm characterize the image. Any carbon dissolution or blistering process is visible and the whole morphology is in close agreement with pristine HOPG (see Figure 18).

The HOPG stability in hydrochloric solution is also demonstrated by the EC-STM structural analysis. The atomic-resolution image (see the inset of Figure 33) shows the traditional graphite corrugation [(0.45 ± 0.08) Å] and no nano-protrusion affects the STM image.

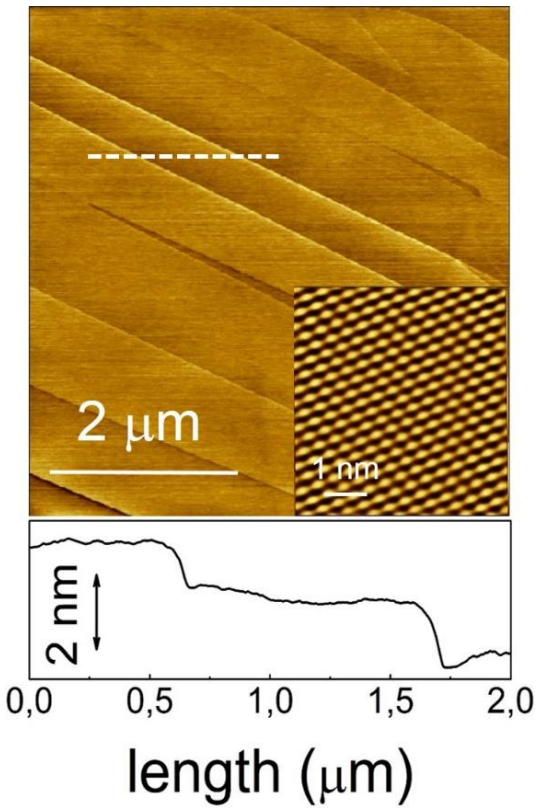

***Figure 33**. EC-AFM topography (5 x 5 μm^2) acquired on graphite immersed in 2 M HCl solution, after a single CV sweep. Atomic resolution [EC-STM (5 x 5 nm^2; I_{tunnel} = 1 nA; V_{bias} = 0.3 V)] is reported in the inset. At the bottom, scan profile of the graphite terraces along the white dashed line.*

3.6 *HOPG OXIDATION IN DILUTED ACID ELECTROLYTES: DISCUSSION*

In the light of the collected results, the comparison between class 2 and class 1 electrolytes demonstrates that nano-protrusion and surface blistering are characteristic of sulfate and perchlorate anion intercalation. In particular, Figures 23 and 27 prove that nano-protrusions affect both blisters (or blister clusters) and flat graphite surfaces, respectively.

I speculate that nano-protrusion can be thought in terms of an incipient blister, which can growth and increase its sizes. Both nano-protrusions and blisters are mechanically stable even when the WE is removed from the EC cell, suggesting that the strained surface is equilibrated by an inner pressure (p_{int}) of the HOPG swelling. p_{int} is produced after the oxidation of solvated anions inside the HOPG crystal, but its value is difficult to calculate. Nano-protrusions look like nano-bubbles produced by Ar [109], where the p_{int} of some GPa is deduced from the Ar trapped between graphene and Ir substrate.

Differently, in our case, three kind of gases are probably produced during graphite oxidation (namely CO, CO_2 and O_2), whose relative amounts are completely unknown. In addition, the volumetric size of nano-bubbles are well defined, while nano-protrusions could extend inside the uppermost graphite layer. Nonetheless, if I hypnotize that nano-protrusions (10 time smaller than nano-bubbles in the exposed volume) are completely confined onto the HOPG surface (single graphene layer), I can estimate in first approximation p_{int}, by considering the Young's modulus for the graphene (*ca* 1 Tpa [115]) and the C-C strein previously estimated by the geometrical construction. The so obtained value of few GPa is in good agreement with the result for the Ar nano-bubbles [109].

An estimation of p_{int} is even more complex if blisters are taken into account, where the number of graphite layers affected by the swelling is still unknown. In

addition, in this case, it is difficult to appreciate a C-C bond stretch from EC-STM images. If blisters are considered, in a very first approximation, in the framework of the Laplace law (mechanical equilibrium in bubbles):

$$p_{int} - p_{ext} \propto \frac{\gamma}{r}$$

where the p_{ext} is approximated to the atmosphere, γ is the mean surface tension for a graphene multilayer (0.1 J/m^2) [116] and $r = 350$ nm (see the blister sizes reported above), the resulting internal pressure consists of only few atmospheres.

This rough estimation requires an experimental evidence as, for instance, stress-strain analysis by EC-AFM. These measurements will be collected in the next future. However, despite the simplicity of the used models, a decreasing p_{int} from nano-protrusion to blisters sustains the basic idea that the latter, with a pressure close to p_{ext}, represent the final stage of the former growth. The coexistence of nano-protrusion on blisters or clusters is beyond this simple mechanical model.

The nano-protrusion and blister evolution is in agreement with the interpretative work in the literature [41]. Here, the authors suggest that step edges and surface defects could be the preferential entrance of solvated anions. **Figure 34** clearly proves this hypothesis following the morphological evolution of the HOPG WE immersed in $HClO_4$ solution as a function of time. Keeping the EC potential in the cell slightly lower than 0.9 V, in order to slow down the anion intercalation rate, I observed that the graphite steps are quickly smoothed and the edges eroded (see the black dashed squares in the figure). In particular, I found that surface holes evolve, showing a progressive broadening within a few minutes (dashed line), while other defects are formed, probably following the carbon dissolution (dashed circles).

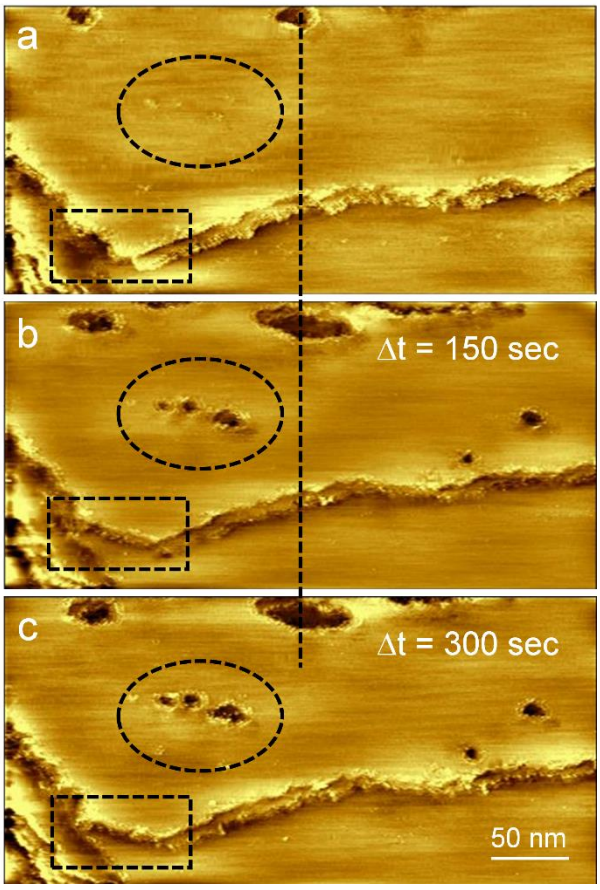

Figure 34. *EC-STM images (I_{tunnel} = 0.7 nA; V_{bias} = 0.8 V) acquired on graphite in $HClO_4$ solution (2 M) at an EC potential just below 0.9 V. The acquisition time of each image (panels a, b and c) is 150 s. The reported Δt refers to the elapsed time computed from the scanning start of the first image (a) to the scanning start of the b) (150 s) or c) (300 s) image. The formation of damages (holes) on the graphite surface is marked by dashed circles. Pre-existing damages increase their sizes (see the dashed straight line). In addition, I observe that the terrace edges are smoothed and the corner eroded, as marked by the dashed squares.*

Carbon dissolution, faceting, edges smoothing, nano-protrusions and blisters represent a very critical phenomenology, because all of them participate to the HOPG basal plane detriment, which limits size and quality of graphene flake production. A stratagem to isolate each process from the others and shine a light on the single molecular mechanism, is offered by the NPV (see Experimental techniques).

4.1 H_2SO_4/HOPG SURFACE EVOLUTION ANALYZED BY NPV

The NPV analysis was used for studying the H_2SO_4 (1 M)/HOPG system. The latter was chosen as a model case for the class 2 electrolytes, because the IV and III intercalation stages are placed at well defined EC potentials (1.1 V and 1.2 V, respectively) and the related traditional CV shows a high reproducibility. These aspects help in defining the precise potential at which the pulse should be set to induce a desired process.

Three EC potentials are chosen: 0.7 V, 1.0 V and 1.2 V, which are values representative of the three faradaic current intervals observed in CV (see Figure 21). The pulse width minimum is $\tau = 0.2$ s (τ-pulse), accordingly to the discussion reported in the Experimental technique chapter.

After many preliminary tests, I observed that if an EC process (e.g. blistering) affects the WE surface after N $\times$ τ-pulses (total time duration $\Delta t = N\tau$) at a defined V_{EC}, blisters are also found if a single pulse of $\Delta t = N\tau$ seconds is applied at the same EC potential. This means that only the total time interval Δt plays a crucial role in the HOPG surface changes. The use of a minimum τ-pulse, which can be repeated N times, helps in finding quickly the *effective* time of an EC process at a defined V_{EC} (e.g. blistering: $t_{blister}$). The latter is defined as the minimum time interval required to observe statistically blisters on the HOPG surface, allowing a quantification of the process kinetics.

The WE, initially at $V_{EC} = 0.3$ V, was set at 1.2 V for a time interval of 0.2 s (τ-pulse, see **Figure 35**) and then reported at 0.3 V. After the pulse, the HOPG surface was studied by the EC-STM, as reported in **Figure 36**.

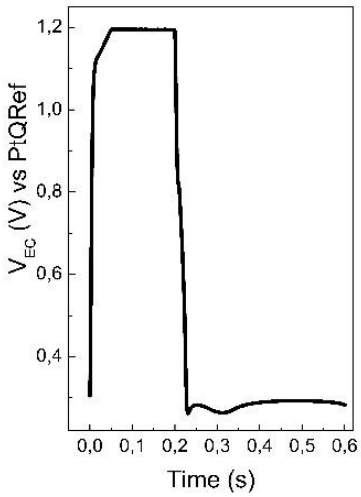

***Figure 35**. Characteristic V_{EC} vs time curve of a τ-pulse. Initial potential = 0.3 V; step potential = 1.2 V; duration = 0.2 s; sampling interval = 0.001 s.*

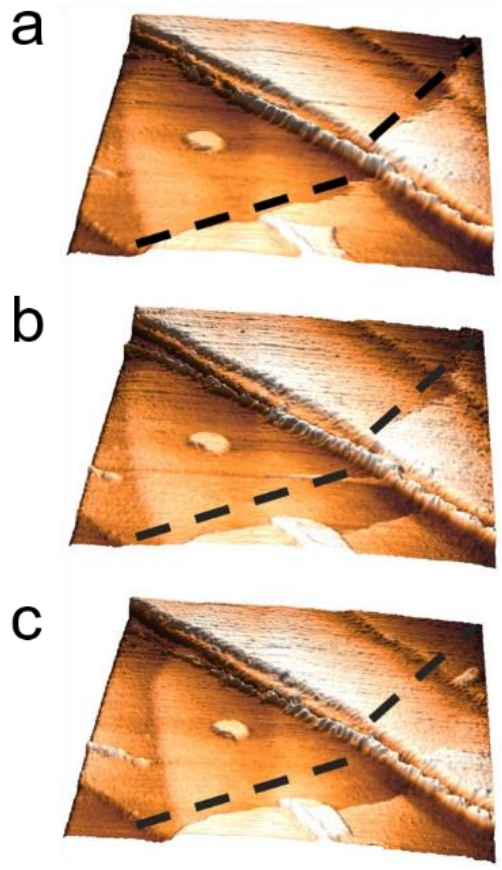

***Figure 36**. EC-STM (500 x 500 nm^2) images (I_{tunnel} = 1.0 nA; V_{bias} = 0.3 V). a) image acquired at V_{EC} = 0.3 V after a pulse of 0.2 s at 1.2 V. The dashed black lines mark the edges of two terraces. b) image acquired after about 60 s from the previous one (a). The terrace dissolution is clear from a direct comparison of the edges with the black dashed lines. c) image acquired 120 s after the (a) image.*

Progressive dissolution of terraces is observed as a function of time, which continues for some minutes after the application of the τ-pulse, worsening the quality of the HOPG basal plane even at 0.3 V. A statistical analysis on different areas of the WE confirms the detriment of the sample.

Incidentally, I observe that no HOPG swellings or blisters are present on the surface. This situation is unchanged after a second pulse of 2τ s (total Δt = 0.6 s) at 1.2 V, as demonstrated by **Figure 37**. Here, the dashed lines emphasize the residuals of an original graphite terrace, which is almost completely dissolved.

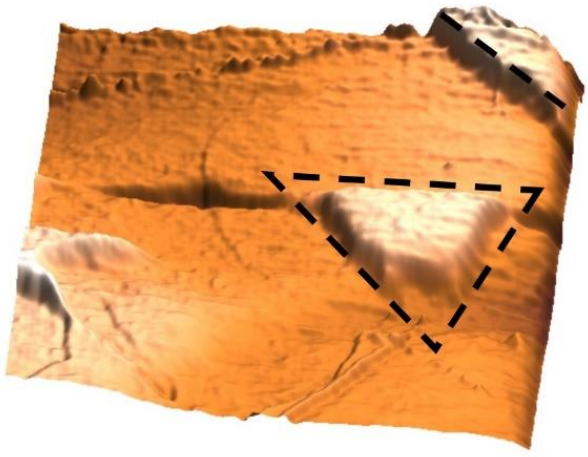

***Figure 37**. EC-STM (300 × 300 nm^2) image of HOPG surface after a second pulse of 0.4 s (total Δt = 0.6 s) at 1.2 V (I_{tunnel} = 1 nA, V_{bias} = 0.3 V). The dashed black line emphasizes the residual of an original graphite terrace, which is almost completely dissolved.*

When the total pulse time Δt is between 0.8 s and 1.6 s, blistering joins the carbon dissolution process, as observed in **Figure 38** (here, only part of a blister is visible on the left-bottom corner of the image). These blisters show smaller sizes (lateral width of only 100 nm and a height of about 5 nm) compared with those acquired after a CV (see Figure 23). I interpret these incipient structures as due to the first growth stages of those blisters that, keeping the sample at 1.2 V for a longer time, evolve in the huge structures reported and discussed above.

***Figure 38**. EC-STM (300 × 300 nm^2) image of HOPG graphite after a total pulse of 1.6 s at 1.2 V (I_{tunnel} = 1 nA; V_{bias} = 0.3 V). The dashed black line emphasizes edge dissolution and HOPG swelling due to a blister (left-bottom corner).*

Blisters start to characterize statistically EC-STM images after a pulse of 1.6 s. Consequently, I define $t_{blister}$ = 1.6 s as the *effective* time for surface blistering. After a total interval time of 3.2 s at 1.2 V, the HOPG surface is completely covered by blisters, as proved by **Figure 39**.

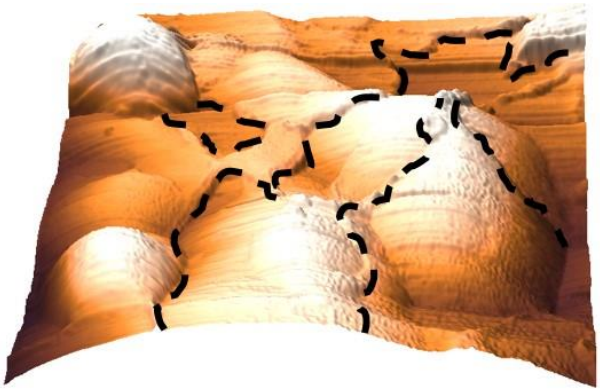

***Figure 39**. EC-STM (300 x 300 nm^2) image after a total pulse of 3.2 s at 1.2 V (I_{tunnel} = 1.0 nA; V_{bias} = 0.3 V). The surface morphology is clearly characterized by swelled graphite terraces and blisters. Black dashed lines mark the graphite dissolution phenomenon on top of blisters.*

Interestingly, I note that these results are in agreement with data acquired after the traditional CV, where blisters affect the HOPG surface after a single potential sweep. In fact, by considering the CV scan rate (see for example Figure 21), the time interval (t_0) spent by the WE at around 1.2 V is about 6 s > $t_{blister}$. As a countercheck, if we impose $t_{dissolution} < t_0 < t_{blister}$, being $t_{dissolution}$ = 0.2 s (see above), the CV scan rate must be set at about 100 mV/s. In **Figure 40**, an EC-STM image was acquired after a CV at $v_{scan\ rate}$ = 100 mV/s. The HOPG surface appears damaged by carbon dissolution but it is completely flat without any swelling.

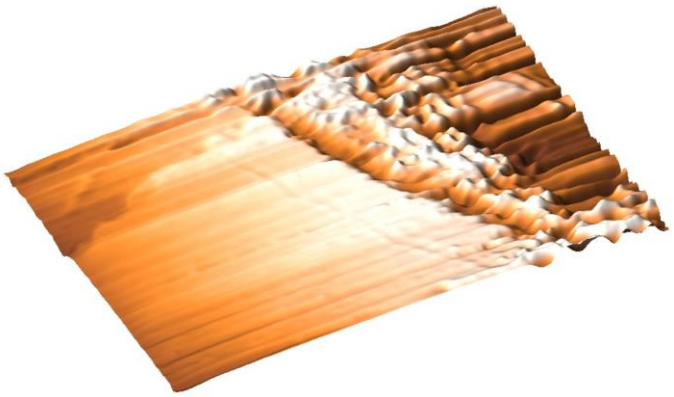

***Figure 40**. EC-STM (500 x 300 nm^2) image after a single CV sweep ($v_{scan\ rate}$ = 100 mV/s). The HOPG surface appears seriously damaged by carbon dissolution but no blister affects the image.*

In the framework of the Murray intercalation model, the enhancement of the faradaic current (between 0.9 V and 1.1 V in Figure 21) does not strictly represent an intercalation stage (the IV being placed at 1.1 V). Consequently, blisters evolution time is expected here longer than $t_{blister}$ = 1.6 s, measured at V_{EC} = 1.2 V. Finding an effective formation time 4 times faster at 1.0 V is thus completely unexpected! **Figure 41** shows surface swelling (dashed black line) and part of a blister (left-bottom corner) after a pulse of only Δt = 0.4 s at V_{EC} = 1.0 V.

This unusual behavior of the HOPG swelling creates, on the one hand, some difficulties in the Murray model and requires, on the other, a new interpretative model, that is able to rationalize the acquired results.

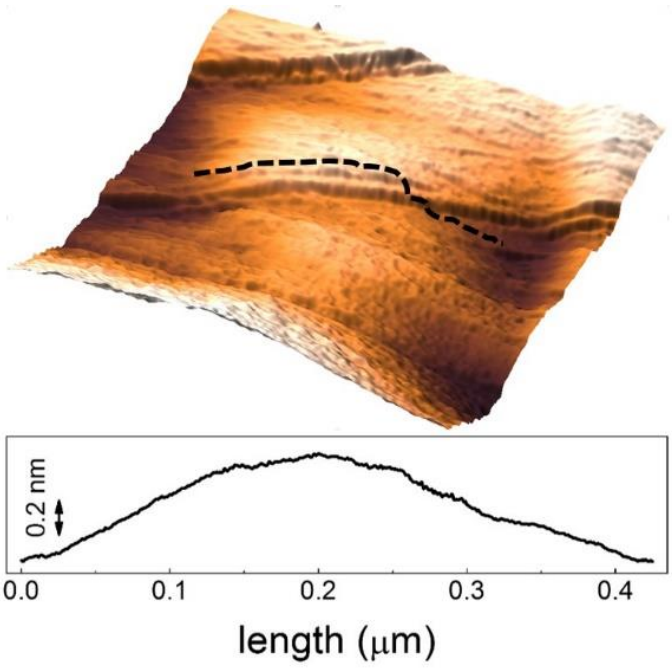

***Figure 41**. EC-STM (500 x 500 nm^2) image after a total pulse of 0.4 s at 1.0 V (I_{tunnel} = 1.0 nA; V_{bias} = 0.3 V). The surface swelling is visible and its profile is reported at the bottom of the image. Part of a blister is observed on the left-bottom corner of the image.*

At this EC potential, HOPG is not affected by an intense carbon dissolution. Step edges are sharp and terrace residuals are not observed in Figure 41. I also checked that the graphite detriment is immaterial even for longer pulse intervals (not reported here).

Finally, the H_2SO_4/HOPG system was analyzed by the NPV applied at 0.7 V. Since at this potential no EC reactions occur on the WE, as measured by the standard CV (null faradic current), no damages of the HOPG basal plane are expected, regardless of the total pulse time used in NPV. As an example, **Figure 42** reveals a regular flat HOPG surface after a total pulse of 1.6 s. Apart some stripes, sometimes observed in diluted H_2SO_4 electrolyte by EC-SPM, the image shows no carbon dissolution, swelling or blistering.

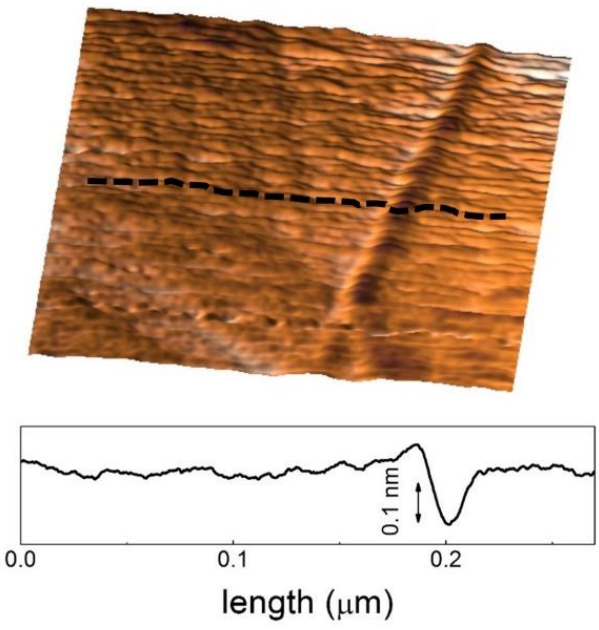

***Figure 42**. EC-STM (300 × 300 nm^2) image acquired after a total pulse of 1.6 s at 0.7 V (I_{tunnel} = 0.8 nA; V_{bias} = 0.3 V). The traditional graphite steps are visible and no damages are present. The profile along the dashed black line is reported at the bottom.*

4.2 *H_2SO_4/HOPG SURFACE EVOLUTION ANALYZED BY NPV: DISCUSSION*

Results obtained by the NPV analysis are precious for the interpretation of the anion intercalation mechanisms of the blistering process. **Table 2** summarizes the experimental data by reporting the effective times of the two main EC processes observed by the EC-SPM investigation (carbon dissolution and surface blistering).

EC process	V_{EC} = 0.7 V	V_{EC} = 1.0 V (onset)	V_{EC} = 1.2 V (III stage)
carbon dissolution	absent	absent	0.2 s
surface blistering	absent	0.4 s	1.6 s

***Table 2**. Rationale of the collected NPV data. The effective times of the observed EC processes are reported.*

When the faradaic current is null in traditional CV (i.e. at 0.7 V), nor dissolution neither blistering are observed in NPV. The HOPG WE is stable immersed in diluted acid electrolytes and any surface delamination is possible.

The graphite surface undergoes a significant detriment when intercalation starts. The above reported data are focused on the III stage, but no differences on the effective times are observed when NPV is applied at 1.1 V (IV stage). Interestingly, I found that $t_{blister}$ can be reduced of a significant percentage (not more of 50%) if the pristine HOPG sample is particularly damaged by steps (e.g.

after hundreds of exfoliations by an adhesive tape), confirming that surface defects are the main entrances of the solvated anions.

However, blisters take the order of few seconds (3.2 s in Figure 39) to cover the HOPG surface. An interesting analysis was performed by Dimiev and co-workers on the GIC formation time [117,118]. By an optical microscope investigation, the authors show that the GIC effective time is of the order of tens of seconds. On the other hand, Lee, Ahn and Ryu found that water intercalation in the graphene/silica interface proceeds with a speed $v = 3\ \mu m/h$ [119]. Assuming, in a first approximation, the same v speed for solvated HSO_4^- anions during graphite intercalation, $t_{blisters}$ corresponds to the required time interval to cross the very first graphite bi-layers, suggesting that the sulfate oxidation and gas evolution are almost instantaneous. Despite the interesting result, v speed is clearly underestimated in this case, because the graphite defects (not taken into consideration) further favor intercalation with the respect to the Lee and co-workers system.

Following the Murray model, CO, CO_2 and O_2 molecules fill blisters. This hypothesis is supported by the collected data. Carbon dissolution of the sample surface is almost instantaneous at IV or III stage potential (see Figure 36). It is reasonable to assume then, that dissolution also affects those inner graphite layers joined by intercalated anions. In this case, in fact, the environment around an inner or a surface carbon atom is comparable (see Figure 3 of the Introduction) and similar processes are expected.

The described mechanisms involved during anion intercalation (first step of a graphite delamination) represent an important drawback in graphene production. The HOPG surface detriment continues for few minutes after a short pulse (see Figure 36), damaging the graphene flakes and limiting the exploitable area for applications. Each delamination procedure requires an intercalation phase, the latter being always joined together with graphite dissolution.

An unexpected stratagem to overcome this bottleneck is offered by surface blistering at lower EC potential (namely 1.0 V), where HOPG is not affected by dissolution. Nonetheless, this result is difficult to rationalize in the Murray framework. In fact, according to this model, anion intercalation is not expected at EC potential below 1.1 V (IV stage).

I note that 1.0 V corresponds to the oxygen overpotential[12] for an HOPG electrode immersed in sulfuric acid electrolyte (see fig. 4 in Ref. 120). Oxygen evolution in the inner cavities of graphite can reasonably swell the pristine HOPG basal plane. If HSO_4^- is ruled out from intercalation, the hydroxyl group (OH^-) is the only electroactive species that can exchange charges at the WE, accordingly to the following equation:

$$4OH^- \rightarrow 2H_2O + O_2 + 4e^-$$

This picture is confirmed by the CV (not reported here). If the WE undergoes a single EC potential sweep up to 0.95 V, the voltammogram is almost flat and no cathodic features (de-intercalation process) are observed. The latter appear as soon as the EC potential reaches 1.0 V, suggesting that (OH^-) intercalation starts. Some EC-STM investigations at 1.0 V are currently underway.

Finally, when the WE is set to 1.2 V, hydroxyl groups intercalation is joined by sulfate anions. The latter could cramp the process, delaying blistering from 0.4 s to 1.6 s.

[12] The overpotential is the difference between the electrode potential under the passage of a current and the thermodynamic value of the electrode potential in the absence of electrolysis.

4 CONCLUSION

Nowadays, 2-D electronics requires flat, flexible and resistant devices and graphene has proved to be the proper material for electronics development. In this respect, huge amount of high-quality graphene flakes are required for electronic device commercialization and the EC graphite delamination represents a concrete strategy to produce graphene. Intercalation of molecules inside the stratified structure of HOPG reduces the layer-layer interaction, favoring the graphite delamination. Despite the very good results obtained in terms of graphene sheet sizes and quality, a significant percentage of flakes results damaged and with a radius below 1 μm. In view of a further improvement of graphene production, research must focus on the molecular mechanisms of anion intercalation and follow the surface evolution of the pristine HOPG crystal, when immersed in diluted acid electrolytes. Unfortunately, the present interpretative model of intercalation results insufficient in explaining the mechanisms, when investigated at the nano-scale.

In this thesis, I propose a combined EC and SPM investigation applied to 2 classes of acids (sulfuric and phosphoric, respectively), trying to overcome the difficulties met by previous researches. In particular, the use of NPV revealed its potentiality in discriminating different processes acting on the HOPG surface at different EC potentials. In the Introduction of this work, I reported some open questions that now, in the light of the collected data, can find an answer.

I unambiguously proved that step edges and surface defects are preferential entrances for anions. The high EC potential, traditionally used for intercalation, dissolves carbon and produces a significant detriment of the graphite basal plane, limiting the quality of the graphene flakes produced. On the other hand, carbon dissolution creates new defects and holes on the HOPG surface, which promote anion intercalation.

Blistering affects the HOPG surface and shows a strained graphite structure that reasonably relaxes after the graphite delamination, as supported by the literature on graphene flakes. Blisters are stable and cover the electrode surface in few seconds. Their stability is obtained by an equilibrium between the strained lattice and the inner pressure. The latter is produced by CO, CO_2, O_2 molecules. In particular, I gave full evidence that carbon dissolution can sustain the formation of CO and CO_2.

The overall picture of anion intercalation seems to be not challenging because HOPG detriment significantly affects each intercalation stage, precluding a further optimization of graphene production. The NPV analysis has disclosed unexpected phenomena that could overcome the apparent bottleneck described above. In fact, an intercalation process is observed at lower potentials, where oxygen evolution starts but carbon dissolution is immaterial. This occurrence was not considered within the traditional intercalation model. In this thesis work, I proposed that hydroxyl groups intercalate inside the graphite, at lower EC potential, favoring the surface swelling. When sulfate (or perchlorate) anions start intercalation (IV and III stages), they indeed represent obstacles in the OH^- and HSO_4^- (or ClO_4^-) co-intercalation and, as a consequence, the blistering time formation is delayed.

Some perspectives of this research can be outlined.

Morphological and structural changes at oxygen overpotential regime are currently in progress and require further investigations. In particular, being hydroxyl groups present in all the used EC solutions, the blister effective time should be the same if the oxygen overpotential onset is reached by the WE. This constrain was realized during the sulfuric and perchloric analysis, but electrolytes belonging to class 1 did not fulfill this requirement. In fact, phosphoric and hydrochloric solutions show a faradaic current enhancement (compatible with an incipient intercalation process, see Figures 29 and 32) but no cathodic features

(de-intercalation) are observed, suggesting that the EC analysis should be extended towards higher potentials.

After blistering at 1.0 V, graphite delamination should be tested. This means that the OH^--intercalated graphite should be immersed in an ultra-sonic bath to facilitate the graphene flake production. The latter could be then compared (sizes, quality, timing, etc.) with flakes produced by the traditional protocol at 1.2 V.

A comparison between the mechanical properties of blisters (stress-strain curves) produced at different EC potentials, is still missing; instead, it could clarify differences between blisters filled by only O_2 and those, where also CO and CO_2 molecules are enclosed.

Finally, other electrolytes could be investigated in view of finding a better compromise between anion intercalation and carbon dissolution.

5 REFERENCE

(1) Reddy, A.L.M.; Srivastava, A.; Gowda, S.R.; Gullapalli, H.; Dubey, M.; Ajayan, P.M. Synthesis of nitrogen-doped graphene films for lithium battery application. *ACS Nano* **2010**, 4(11), 6337–6342.

(2) Koehne, J.; Chen, H.; Li, J.; Cassell, A. M; Ye, Q.; Ng, H. T; Han, J.; Meyyappan, M. Ultrasensitive label-free DNA analysis using an electronic chip based on carbon nanotube nanoelectrode arrays. *Nanotechnol*. **2003**, 14, 1239-1245.

(3) Besenhard, J.O.; Fritz, H.P. The electrochemistry of black carbons. *Angew. Chem., Int. Ed. Engl.* **1983**, 22(12), 950–975.

(4) Crevillen, A.G.; Pumera, M.; Gonzalez, M.C.; Escarpa, A. The preferential electrocatalytic behaviour of graphite and multiwalled carbon nanotubes on enediol groups and their analytical implications in real domains. *Analyst* **2009**, 134(4), 657–662.

(5) Saito, R.; Fujita, M.; Dresselhaus, G.; Dresselhaus, M.S. Electronic structure of chiral graphene tubules. *Appl. Phys. Lett*. **1992**, 60(18), 2204.

(6) Jouikov, V.; Simonet, J. Novel method for grafting alkyl chains onto glassy carbon. Application to the easy immobilization of ferrocene used as redox probe. *Langmuir* **2012**, 28(1), 931–938.

(7) González Orive, A.; Grumelli, D.; Vericat, C.; Ramallo-López, J.M.; Giovanetti, L.; Benitez, G.; Azcárate, J.C.; Corthey, G.; Fonticelli, M.H.; Requejo, F.G.; Hernández Creus, A.; Salvarezza, R.C. 'Naked' gold nanoparticles supported on HOPG: melanin functionalization and catalytic activity. *Nanoscale* **2011**, 3(4), 1708–1716.

(8) Aoki, M.; Amawashi, H. Dependence of band structures on stacking and field in layered graphene. *Solid State Commun*. **2007**, 142, 123–127.

(9) Trucano, P.; Chen, R. Structure of graphite by neutron diffraction. *Nature* **1975**, 258, 136.

(10) Bernal, J.D. The Structure of Graphite. *Proc. R. Soc. London, Ser. A* **1924**, 106, 749–773.

(11) Alkire R. C.; Bartlett P. N.; Lipkowski J. Advances in Electrochemical Science and Engineering Vol. 16, Wiley, New York (**2015**).

(12) Reich, S.; Thomsen, C. Raman spectroscopy of graphite. *Philos. Trans. R. Soc. London, Ser. A* **2004**, 362, 2271–2288.

(13) Data obtained from © Optigraph GmbH Web page.

(14) Spanu, L.; Sorella, S.; Galli, G. Nature and Strength of Interlayer Binding in Graphite. *Phys. Rev. Lett.* **2009**, 103, 196401.

(15) Lee, C.; Wei, X.; Kysar, J.W.; Hone, J. Measurement of the Elastic Properties and Intrinsic Strength of Monolayer Graphene. *Science* **2008**, 321, 385–388.

(16) Tománek, D. and Louie, S.G. First-principles calculation of highly asymmetric structure in scanning-tunneling-microscopy images of graphite. *Phys. Rev. B* **1988**, 37, 8327–8336.

(17) Jayasena, B.; Subbiah, S. A novel mechanical cleavage method for synthesizing few-layer graphenes. *Nano. Res. Lett.* **2011**, 6(95), 1-7.

(18) Lapshin, R.V. Automatic lateral calibration of tunneling microscope scanners. *Rev. Sci. Instrum.* **1998**, 69(9), 3268.

(19) Binnig, G.; Quate, C.F.; Gerber, C. Atomic Force Microscope. *Phys. Rev. Lett.* **1986**, 56, 930–933.

(20) McCreery, R.L. Carbon electrodes: structural effects on electron transfer kinetics, in Electroanalytical Chemistry, vol. 17, Marcel Dekker, New York (**1991**).

(21) McCreery, R.L. Advanced Carbon Electrode Materials for Molecular Electrochemistry. *Chem. Rev.* **2008**, 108, 2646–2687.

(22) Xia, J.; Chen, F.; Li, J.; Tao, N. Measurement of the quantum capacitance of graphene. *Nat. Nanotechnol.* **2009**, 4, 505–509.

(23) Zhong, J. H.; Liu, J. Y.; Li, Q.; Li, M. G.; Zeng, Z. C.; Hu, S.; Wu, D. Y.; Cai, W.; Ren, B. Interfacial capacitance of graphene: Correlated differential capacitance and in situ electrochemical Raman spectroscopy study. *Electrochim. Acta* **2013**, 110, 754–761.

(24) Rice, R.J.; Pontikos, N.M.; McCreery, R.L. Quantitative correlations of heterogeneous electron-transfer kinetics with surface properties of glassy carbon electrodes. *J. Am. Chem. Soc.* **1990**, 112, 4617–4622.

(25) Cline, K.K.; McDermott, M.T.; McCreery, R.L. J. Anomalously Slow Electron Transfer at Ordered Graphite Electrodes: Influence of Electronic Factors and Reactive Sites. *Phys. Chem.* **1994**, 98, 5314–5319.

(26) Brownson, D. A. C.; Banks, C. E. The Handbook of Graphene Electrochemistry, Ch. 2, Springer, Berlin (**2014**).

(27) Dreyer, D. R.; Park, S.; Bielawski, C. W.; Ruoff, R. S. The chemistry of graphene oxide. *Chem. Soc. Rev.* **2010**, 39, 228.

(28) Shih, C. J. et al. Bi- and trilayer graphene solutions. *Nat. Nanotechnol.* **2011**, 6, 439.

(29) Nicolosi, V.; Chhowalla, M.; Kanatzidis, M. G.; Strano, M.S.; Coleman, J. N. Liquid Exfoliation of Layered Materials. *Science* **2013**, 340, 1226419.

(30) Eda, G. et al. Photoluminescence from chemically exfoliated MoS_2. *Nano Lett.* **2011**, 11, 5111.

(31) Xia, Z. Y. et al. The Exfoliation of Graphene in Liquids by Electrochemical, Chemical, and Sonication-Assisted Techniques: A Nanoscale Study. *Adv. Funct. Mater.* **2013**, 23, 4684-4693.

(32) Qi, B.; He, L.; Bo, X.; Yang, H.; Guo, L. Electrochemical preparation of free-standing few-layer graphene through oxidation–reduction cycling. *Chem. Eng. J.* **2011**, 171, 340-344.

(33) Kinoshita, K. Carbon. Electrochemical and Physicochemical Properties. Wiley, New York (**1988**).

(34) Dresselhaus, M. S.; Endo, M. Graphite Intercalation Compounds II. Springer, Berlin (**1992**).

(35) Zheng, T.; Reimers, J.N.; Dahn, J.R. Effect of turbostratic disorder in graphitic carbon hosts on the intercalation of lithium. *Phys. Rev. B* **1995**, 51(2), 734-741.

(36) Alliata, D. Investigation of Nanoscale intercalation into graphite and carbon materials by in situ Scanning Probe Microscopy. *PhD Thesis*, Berna (**2000**).

(37) Singh, P. R.; Zeng X. Size-Dependent Intercalation of Ions into Highly Oriented Pyrolytic Graphite in Ionic Liquids: An Electrochemical Atomic Force Microscopy Study. *J. Phys. Chem. C* **2011**, 115, 17429–17439.

(38) Beck, F.; Krohn H. Reversible Electrochemical Intercalation of Anions from Aqueous Solutions in Polymer Bound Graphite Electrodes. *Synth. Met.* **1983**, 7, 193 – 199.

(49) Goss, C. A.; Brumfield, J. C.; Irene, E. A.; Murray, R. W. Imaging the Incipient Electrochemical Oxidation of Highly Oriented Pyrolytic Graphite. *Anal. Chem.* **1993**, 65, 1378−1389.

(40) Hathcock, K. W.; Brumfield, J. C.; Goss, C. A.; Irene, E. A.; Murray, R. W. Incipient Electrochemical Oxidation of Highly Oriented Pyrolytic Graphite: Correlation between Surface Blistering and Electrolyte Anion Intercalation. *Anal. Chem.* **1995**, 67, 2201 -2206.

(41) Alsmeyer, D.C.; McCreery, R.L. In Situ Raman Monitoring of Electrochemical Graphite Intercalation and Lattice Damage in Mild Aqueous Acids. *Anal. Chem.* **1992**, 64, 1528–1533.

(42) Zhang, B.; Wang, E. Effects of Anodic Oxidation on the Surface Structure of Highly Oriented Pyrolytic Graphite Revealed by In Situ Electrochemical Scanning Tunneling Microscopy in H_2SO_4 Solution. *Electrochim. Acta* **1995**, 40, 2627−2633.

(43) Schnydera, B.; Alliata, D.; Kötz, R.; Siegenthaler H. Electrochemical intercalation of perchlorate ions in HOPG: an SFM/LFM and XPS study. *Appl. Surf. Sci.* **2001**, 173, 221-232.

(44) Bussetti, G.; Yivlialin, R.; Alliata, D.; Li Bassi, A.; Castiglioni, C.; Tommasini, M.; Casari, C. S.; Passoni, M.; Biagioni, P.; Ciccacci, F.; Duò, L. Disclosing the Early Stages of Electrochemical Anion Intercalation in Graphite by a Combined Atomic Force Microscopy/Scanning Tunneling Microscopy Approach. *J. Phys. Chem. C* **2016**, 120, 6088−6093.

(45) Bard, A.J.; Faulkner, L. Electrochemical Methods. Wiley, New York (**2001**).

(46) Bagotsky, V.S. Fundamentals of Electrochemistry. Wiley, New York (**2005**).

(47) Gulaboski, R.; Pereira C. M. Electroanalytical Techniques and Instrumentation in Food Analysis. Handbook of Food Analysis Instruments, CRC Press, Boca Raton (**2009**).

(48) Pyun, S. I.; Shin, H. C.; Lee, J. W.; Go, J. Y. Electrochemistry of Insertion Materials for Hydrogen and Lithium. Springer, Berlin (**2012**).

(49) Kissinger, P. T.; Heineman, W. R. Cyclic Voltammetry. *J. Chem. Educ.* **1983**, 60(9), 702.

(50) Brett, C. M. A.; Brett, A. M. O. Electrochemistry Principles, Methods, And Applications. Oxford University Press, New York (**1993**).

(51) Reiss, H.; Heller, A. The Absolute Potential of the Standard Hydrogen Electrode: A New Estimate *J. Phys. Chem.* **1985**, 89, 4207-4213.

(52) Inzelt, G.; Lewenstam, A.; Scholz, F. Handbook of Reference Electrodes. Springer, Berlin (**2013**).

(53) Fick A. On liquid diffusion. *J. Membr. Sci.* **1995**, 100, 33-38.

(54) Kooijman, H. A. A Modification of the Stokes-Einstein Equation for Diffusivities in Dilute Binary Mixtures. *Ind. Eng. Chem. Res.* **2002**, 41, 3326-3328.

(55) Bauer, H. H.; Christian, G. D.; O'Reilly J. E. Analisi strumentale. Piccin (**1985**).

(56) Beck, F.; Junge, H.; Krohn, H. Graphite Intercalation Compounds As Positive Electrodes In Galvanic Cells. *Electrochim. Acta* **1981**, 26, 799-809.

(57) Grahame, D. C. The Electrical Double Layer And The Theory Of Electrocapillarity. *Chem. Rev.* **1947**, 41(3), 441–501.

(58) Shahrokhian, S.; Asadian, E. Simultaneous voltammetric determination of ascorbic acid, acetaminophen and isoniazid using thionine immobilized multi-walled carbon nanotube modified carbon paste electrode. *Electrochim. Acta* **2010**, 55, 666–672.

(59) Binnig, G.; Rohrer, H.; Gerber, C.; Weibel, E. Tunneling through a Controllable Vacuum Gap. *Appl. Phys. Lett.* **1982**, 40, 178-180.

(60) Binnig, G.; Rohrer, H.; Gerber, C.; Weibel, E. Surface Studies by Scanning Tunneling Microscopy. *Phys. Rev. Lett.* **1982**, 49, 57-61.

(61) Frommer, J. Scanning tunneling microscopy and atomic force microscopy in organic chemistry. *Angew. Chem. Int. Ed.* **1992**, 31, 1298-1328.

(62) Samori, P. Scanning probe microscopies beyond imaging. *J. Mater. Chem.* **2004**, 14, 1353-1366.

(63) Kolb, D.M.; Simeone, F.C. Electrochemical nanostructuring with an STM: A status report. *Electrochim. Acta* **2005**, 50, 2989-2996.

(64) Bard, A.J.; Fan, F.R. Introductory lecture studies of the liquid-solid interface by scanning-Tunneling-microscopy and scanning electrochemical microscopy. Faraday Discuss. **1992**, 94, 1-22.

(65) Sonnenfeld, R.; Hansma, P.K. Atomic-resolution microscopy in Water. *Science* **1986**, 232, 211-213.

(66) Hansma, P.K.; Tersoff, J. Scanning tunneling microscopy. *J. Appl. Phys.* **1987**, 61, 1-23.

(67) Hansma, P.K.; Elings, V.B.; Marti, O.; Bracker, C.E. Scanning tunneling microscopy and atomic force microscopy: Application to biology and technology. *Science* **1988**, 242, 209-216.

(68) Itaya, K.; Tomita, E. Scanning tunneling microscope for electrochemistry-A new concept for the In situ scanning tunneling microscope in electrolyte solutions. *Surf. Sci.* **1988**, 201, 507-512.

(69) Itaya, K. In situ scanning tunneling microscopy in electrolyte solutions. *Prog. Surf. Sci.* **1998**, 58, 121-247.

(70) Wilms, M.; Kruft, M.; Bermes, G.; Wandelt, K. A new and sophisticated electrochemical scanning tunneling microscope design for the investigation of potentiodynamic processes. *Rev. Sci. Instrum.* **1999**, 70, 3641-3650.

(71) Yagati, A. K.; Min, J.; Choi J.W. Electrochemical Scanning Tunneling Microscopy (ECSTM) – From Theory to Future Applications. Modern Electrochemical Methods in Nano, Surface and Corrosion Science, INTECH (**2014**).

(72) Díez-Péreza, I.; Sanza, F.; Gorostizab, P. In situ studies of metal passive films. *Curr. Opin. Solid State Mater. Sci.* **2006**, 10, 144-152.

(73) Kabasakaloğlu, K.; Kiyak, T.; Sendil, O.; Asan, A. Electrochemical behavior of brass in 0.1 M NaCl. *Appl. Surf. Sci.* **2002**, 193(1-4) 167-174.

(74) Zamborni, F. P.; Crooks, R. M. Corrosion passivation of gold by n-alkanethiol self-assembled monolayers: Effect of chain length and end group. *Langmuir* **1998**, 14(12), 3279-3286.

(75) Hai, N.T.M.; Kosmala, T.; Wandelt, K. Potential dependence of self-assembled porphyrin layers on a Cu(111) electrode surface: In-situ STM study. *Surf. Sci.* **2015**, 631, 207–212.

(76) Goletti, C.; Bussetti, G.; Violante, A.; Bonanni, B.; Di Giovannantonio, M.; Serrano, G.; Breuer, S.; Gentz, K.; Wandelt, K. Cu(110) Surface in Hydrochloric Acid Solution: Potential Dependent Chloride Adsorption and Surface Restructuring. *J. Phys. Chem. C* **2015**, 119, 1782−1790.

(77) Gittins, D. I.; Bethell, D.; Schiffrin, D. J.; Nichols R. J. A nanometre-scale electronic switch consisting of a metal cluster and redox-address able groups. *Nature* **2000**, 408, 67-69.

(78) Kim S.U.; Yagati, A.K.; Min, J.; Choi, J.W. Nanoscale protein-based memory device composed of recombinant azurin. *Biomaterials* **2010**, 31(6), 1293-1298.

(79) Artes, J.M; Diez-perez I; Sanz, F.; Gorostiza P. Direct measurement of electron transfer distance decay constants of single redox proteins by electrochemical tunneling spectroscopy. *ACS Nano* **2011**, 5(3), 2060-2066.

(80) Tersoff, J.; Hamann, D. R. Theory and Application for the Scanning Tunneling Microscope. *Phys. Rev. Lett.* **1983**, 50(25), 1998-2001.

(81) Oura K.; Lifshits V.; Saranin A.; Zotov A.; Katayama M. Surface Science An introduction, Springer, Berlin (**2003**).

(82) Hallmark, V.M; Chiang, S.; Rabolt, J.F.; Swalen, J.D.; Wilson, R.J. Observation of Atomic Corrugation on Au(111) by Scanning Tunneling Microscopy. *Phys. Rev. Lett.* **1987**, 59, 2879-2882.

(83) Auwärter, W.; Seufert, K.; Bischoff, F.; Ecija, D.; Vijayaraghavan, S.; Joshi, S.; Klappenberger, F.; Samudrala, N.; Barth, J. V. A surface-anchored molecular four-level conductance switch based on single proton transfer. *Nature Nanotechnology* **2012**, 7, 41-47.

(84) Tersoff, J.; Hamann. Theory of scanning tunneling microscope. *Phys. Rev. B* **1985**, 31, 805-813.

(85) Hla, S.W. Scanning tunneling microscopy single atom/molecule manipulation and its application to nanoscience and technology. *J. Vac. Sci. Technol. B* **2005**, 23, 1351-1360.

(86) Meyer, G.; Amer, N. M. Novel optical approach to atomic force microscopy. *Appl. Phys. Lett.* **1988**, 53, 1045-1047.

(87) Pethica, J. B.; Oliver, W. C. Tip Surface Interactions in STM and AFM. *Physica Scripta*. 1987, T19, 61-66.

(88) Kouzeki, T.; Tatezono, S.; Yanagi, H. Electrochromism of Orientation-Controlled Naphthalocyanine Thin Films. *J. Phys. Chem*. **1996**, 100, 20097-20102.

(89) Manne, S.; Gaub, H. E. Molecular organization of surfactants at solid-liquid interfaces. *Science* **1995**, 270.5241, 1480.

(90) Roiter, Y.; Minko, S. AFM Single Molecule Experiments at the Solid−Liquid Interface: In Situ Conformation of Adsorbed Flexible Polyelectrolyte Chains. *J. Am. Chem. Soc.* **2005**, 127 (45), 15688–15689.

(91) Henderson, E.; Haydon, P. G.; Sakaguchi, D. S. Actin filament dynamics in living glial cells imaged by atomic force microscopy. *Science* **1992**, 257, 1944-1946.

(92) Radmacher, M. Measuring the elastic properties of biological samples with the AFM. *IEEE Engineering in Medicine and Biology Magazine* **1997**, 16, 47-57.

(93) Lennard-Jones, J. E. Cohesion. *Proc. Phys. Soc.* **1931**, 43, 461-482.

(94) Cappella, B.; Dietler G. Force-distance curves by atomic force microscopy. *Surf. Sci. Rep.* **1999**, 34, 1-104.

(95) Bradley, R.S. The Cohesive Force between Solid Surfaces and the Surface Energy of Solids. *Phil. Mag.* **1932**, 13, 853-862.

(96) Derjaguin, B. V.; Muller, V. M.; Toporov, Y. P. Effect of contact deformations on the adhesion of particles. *J. Colloid Interface Sci.* **1975**, 53, 314-326.

(97) Johnson, K. L.; Kendall, K.; Roberts, A. D. Surface Energy and the Contact of Elastic Solids. *Proc. Roy. Soc. A* **1971**, 324, 301-313.

(98) Giessibl, F. J. Advances in atomic force microscopy. *Rev. Mod. Phys.* **2003**, 75, 949-983.

(99) Teflon PTFE – fluoropolymer resin. *Properties handbook*, DuPont.

(100) Skoog, D. A.; Holler, J. F.; Crouch S. R. Chimica analitica strumentale, Edises (**2009**)

(101) Alliata, D.; Kötz, R.; Haas, O.; Siegenthaler, H. In-Situ AFM Study of Interlayer Spacing during Anion Intercalation into HOPG in Aqueous Electrolyte. *Langmuir* **1999**, 15, 8483−8489.

(102) Liu, J. et al. A green approach to the synthesis of high-quality graphene oxide flakes via electrochemical exfoliation of pencil core. *RSC Adv.* **2013**, 3, 11745–11750.

(103) Nyamjav, D. The Stm Imaging of The Surface Structure of Graphite.

(104) Nicholson, R. S. Theory and Application of Cyclic Voltammetry for Measurement of Electrode Reaction Kinetics. *Anal. Chem.* **1965**, 37 (11), 1351–1355.

(105) Mabboil, G. A. An Introduction to Cyclic Voltammetry. *J. Chem. Educ.* **1983**, 60(9), 697-702.

(106) Meyer, J. C.; Geim, A. K.; Katsnelson, M. I.; Novoselov, K. S.; Booth, T. J.; Roth, S. The Structure of Suspended Graphene Sheets. *Nature* **2007**, 446, 60−63.

(107) Fasolino, A.; Los, J. H.; Katsnelson, M. I. Intrinsic ripples in graphene. *Nat. Mater*. **2007**, 6, 858−861.

(108) Grantab, R.; Shenoy, V. B.; Ruoff, R. S. Anomalous Strength Characteristics of Tilt Grain Boundaries in Graphene. *Science* **2010**, 330, 946−948.

(109) Zamborlini, G.; Imam, M.; Patera, L. L.; Mentes, T. O.; Stojić, N.; Africh, C.; Sala, A.; Binggeli, N.; Comelli, G.; Locatelli, A. Nanobubbles at GPa under Graphene. *Nano Lett.* **2015**, 15, 6162− 6169.

(110) Rong, Z. Y.; Kuiper, P. Electronic efFects in scanning tunneling microscopy: Moire pattern on a graphite surface. *Phys. Rev. B* **1993**, 48, 17427-17431.

(111) Guenbour, A.; Iken, H.; Kebkab, N.; Bellaouchou, A.; Boulif, R.; Ben Bachir, A. Corrosion of graphite in industrial phosphoric acid. *Appl. Surf. Sci.* **2006**, 252, 8710–8715.

(112) Thiele, H. The oxidation of carbon in electrolytes at normal temperature. *Trans. Faraday Soc.* **1938**, 34, 1033-1039.

(113) Yivlialin, R.; Brambilla, L.; Bussetti, G.; Tommasini, M.; Li Bassi, A.; Casari, C. S.; Passoni, M.; Ciccacci, F.; Duò, L.; Castiglioni, C. Evolution of the graphite surface in phosphoric acid: an AFM and Raman study. *Beilstein J. Nanotechnol.* **2016**, 7, 1878–1884.

(114) Bartoli, A.; Papasogli, G. Sviluppo di eletricità per l'ossidazione a freddo del carbone. *Il Nuovo Cimento* **1882**, 10, 274-277.

(115) Lee, C.; Wei, X.; Kysar, J. W.; Hone, J. Measurement of the Elastic Properties and Intrinsic Strength of Monolayer Graphene. *Science* **2008**, 321, 384-388.

(116) Shih, C.J.; Strano, M. S.; Blankschtein D. Wetting translucency of Graphene. *Nature Mat.* **2013**, 12, 866-869.

(117) Dimiev, A. M. et al. Direct Real-Time Monitoring of Stage Transitions in Graphite Intercalation Compounds. *ACS Nano* **2013**, 7, 2773-2780.

(118) Dimiev, A. M.; Tour, J. M. Mechanism of Graphene Oxide Formation. *ACS Nano* **2014**, **8**, 3060-3068.

(119) Lee, DE.; Ahn, G.; Ryu, S. Two-Dimensional Water Diffusion at a Graphene–Silica Interface. *J. Am. Chem. Soc.* **2014**, 136, 6634-6642.

(120) Tanaka, Y.; Furuta, M.; Kuriyama, K.; Kuwabara, R.; Katsuki, Y.; Kondo, T.; Fujishima, A.; Honda, K. Electrochemical Properties of N-Doped Hydrogenated Amorphous Carbon Films Fabricated by Plasma-Enhanced Chemical Vapor Deposition Methods. *Electrochim. Acta* **2011**, 56, 1172-1181.